

# Molecular Gas Dynamics in NGC 6946: a Bar-driven Nuclear Starburst “Caught in the Act”<sup>1</sup>

Eva Schinnerer

*Max-Planck-Institut für Astronomie, Königstuhl 17, D-69117 Heidelberg, Germany*

`schinner@mpia.de`

Torsten Böker

*European Space Agency, Dept. RSSD, Keplerlaan 1, 2200 AG Noordwijk, Netherlands*

`tboeker@rssd.esa.int`

Eric Emsellem

*CRAL-Observatoire, 9 avenue Charles André, 69231 Saint Genis Laval, France*

`emsellem@obs.univ-lyon1.fr`

and

Ute Lisenfeld

*Dept. Física Teórica y del Cosmos, Facultad de Ciencias, Universidad de Granada, 18071 Granada, Spain and Instituto de Astrofísica de Andalucía, CSIC, Apdo. 3004, 18080 Granada, Spain*

`ute@ugr.es`

## ABSTRACT

We present high angular resolution ( $\sim 1''$  and  $0.6''$ ) mm-interferometric observations of the  $^{12}\text{CO}(1-0)$  and  $^{12}\text{CO}(2-1)$  line emission in the central 300 pc of the late-type spiral galaxy NGC 6946. The data, obtained with the IRAM Plateau de Bure Interferometer (PdBI), allow the first detection of a molecular gas spiral in the inner  $\sim 10''$  (270 pc) with a large concentration of molecular

---

<sup>1</sup>Based on observations carried out with the IRAM Plateau de Bure Interferometer. IRAM is supported by INSU/CNRS (France), MPG (Germany) and IGN (Spain).

gas ( $M_{H_2} \sim 1.6 \times 10^7 M_\odot$ ) within the inner 60 pc. This nuclear clump shows evidence for a ring-like geometry with a radius of  $\sim 10$  pc as inferred from the p-v diagrams. Both the distribution of the molecular gas as well as its kinematics can be well explained by the influence of an inner stellar bar of about 400 pc length. A qualitative model of the expected gas flow shows that streaming motions along the leading sides of this bar are a plausible explanation for the high nuclear gas density. Thus, NGC 6946 is a prime example of molecular gas kinematics being driven by a small-scale, secondary stellar bar.

*Subject headings:* galaxies: nuclei — galaxies: ISM — galaxies: kinematics and dynamics — galaxies: individual(NGC 6946)

## 1. Introduction

A large fraction of nearby spiral galaxies experience intense star formation within a few hundred parsec from their nuclei. Many detailed studies exist of the stellar populations produced in these starbursts and the physical conditions of the ionized gas surrounding them. These studies mostly use imaging and/or spectroscopy at optical and near-infrared (NIR) wavelengths which can provide sub-arcsecond resolution and thus allow the study of star formation processes at scales of individual giant molecular clouds (GMCs). Case studies of this type include NGC 1808 (Krabbe, Sternberg, & Genzel 1994; Tacconi-Garman et al. 1996), IC 342 (Böker, Förster-Schreiber, & Genzel 1997), NGC 253 (Engelbracht et al. 1998), and also the subject of this paper, NGC 6946 (Engelbracht et al. 1996).

A necessary, although maybe not sufficient, condition for such nuclear star formation is the inward transport of molecular gas – the raw material for producing stars – from the outer galaxy disk. If efficient enough, this transport can, over time, lead to a re-distribution of the baryonic mass, and thus can change the appearance of a galaxy, in the sense that the (stellar) mass distribution becomes more centrally concentrated. Recently, such secular evolution processes have received renewed attention, because observational evidence has accumulated that at least at the late-type end of the Hubble sequence, galaxy bulges grow and modify their appearance well after their host disks have formed (for a detailed review see Kormendy & Kennicutt 2004). Without a detailed understanding of the mechanisms that govern the transport of disk gas into the innermost regions of disk galaxies, our understanding of galaxy evolution therefore remains incomplete.

Over the past decades, much progress has been made in the theoretical understanding of the mechanisms that cause gas rotating inside the galaxy disk to lose angular momentum and

to radially drift towards the nucleus. Bars and spirals have often been mentioned as potential drivers for inward gas motion, but the efficiency of such processes is rather badly understood, and certainly depends on the physical state of the gas (e.g. viscosity) and on the detailed characteristics of the acting perturbation (e.g. the pattern speed of the bar Combes & Gerin 1985). Athanassoula (1992) has performed a whole set of hydro-dynamical simulations exploring the influence of the main parameters of the bar: central concentration, axial ratio, quadrupole moment, and pattern speed. At the same time, Combes & Elmegreen (1993) have explored the behavior and appearance of bars in early and late type spirals showing that quite different types of bars are expected for these two classes of galaxies. Direct comparison of models to observations have shown that gas flow induced by stellar bars can, for example, explain the complex kinematics in our Galactic Center (Binney et al. 1991) or the gas flow in the double-barred spiral galaxy M100 where the two nested bars need to be dynamically decoupled (Garcia-Burillo et al. 1998). Recently, (hydro-)dynamical modeling of the gas flow in central kiloparsec by e.g. Englmaier & Shlosman (2000); Maciejewski et al. (2002); Maciejewski (2004b,a) has provided detailed predictions about the properties of the gas in the presence of single or nested bars. In addition, the influence of bars on the gas dynamics has been well-tested by observations on spatial scales of a few kpc, for example in NGC 4303 (Schinnerer et al. 2002), NGC 5383 (Sheth et al. 2000), or NGC 5005 (Sakamoto et al. 2000).

However, relatively little is known about whether similar mechanisms are also at work to produce the high (molecular) gas density required to enable the intense **nuclear** star formation (i.e. inside  $\sim 100$  pc from the dynamical center) observed in many spirals. While it is tempting to invoke small-scale inner bars and dynamical resonances in a way similar to the standard model of kpc-scale starbursts, there are few observational tests of these models on the scales of nuclear starbursts. The reason lies mostly in the fact that maps of the molecular gas can rarely match the angular resolution obtained at optical/NIR wavelengths. For example, the most comprehensive interferometric CO survey of nearby galaxies, the BIMA SoNG (Regan et al. 2001; Helfer et al. 2003), has on average a spatial resolution of  $6''$ , or 300 pc at a distance of 10 Mpc. The IRAM PdBI key project NUGA is reaching angular resolution below  $1''$ : however it is focused on a smaller sample of nearby spiral galaxies containing an active nucleus (García-Burillo et al. 2003). Therefore, it is only in a few nearby (and bright) galaxies that one can hope to obtain a more detailed picture of the molecular gas dynamics within and around the nuclear starbursts, and to observationally constrain dynamical models on scales of a few tens of parsecs.

NGC 6946 provides such an opportunity. At a distance<sup>2</sup> of 5.5 Mpc ( $1'' = 27$  pc Tully

---

<sup>2</sup>The exact distance to NGC 6946 is somewhat uncertain. The Nearby Galaxies Catalog of Tully (1988) reports a distance of 5.5 Mpc, but more recent estimates are  $5.9 \pm 0.4$  Mpc to the center of the NGC 6946 group

1988), it is one of the nearest large spiral galaxies outside the local group, and is currently undergoing intense nuclear star formation (e.g. Engelbracht et al. 1996). The enhanced star formation activity is unlikely to be triggered by a dynamical interaction, since HI observations of the neighborhood of NGC 6946 (Pisano & Wilcots 2000) show neither obvious tidal streams nor any companion galaxies that are massive and close enough to have any dynamical impact on NGC 6946. However, the HI velocity field is not symmetric at the outskirts of the disk (e.g. Crosthwaite 2002). NGC 6946 is classified as an SAB in the RC3 catalog (de Vaucouleurs et al. 1991); a stellar bar with a length of  $\geq 120''$  (3.5 kpc) and position angle of  $17^\circ$  has been identified in NIR images (Regan & Vogel 1995; Menéndez-Delmestre et al. 2006). In addition, and more importantly for the data presented in this paper, NGC 6946 harbors a small inner bar with an estimated major axis diameter of  $\sim 200$  pc which is most clearly visible in the NIR images of Elmegreen et al. (1998) and Knapen et al. (2003). Regan & Vogel (1995) have argued that the inner bar is too small to be responsible for the pile-up of molecular gas in the center of NGC 6946. However, its role for the gas dynamics inside the central  $\sim 100$  pc could not be studied in previous CO observations due to their limited spatial resolution.

In this paper, we present new  $0.6''$  resolution CO maps that reveal in detail the molecular gas flow around (and within) the inner bar. We will use these data, in combination with dynamical models, to demonstrate that NGC 6946 is in fact a showcase for a nuclear starburst that is sustained by bar-driven inflow of molecular gas. We describe our observations and the data reduction procedure in § 2, and present the observational results in § 3. We will compare these results in § 4 to dynamical models of gas flows within the stellar potential (derived from NIR data), and will show that the observed gas morphology is well explained by the model. The relation between the nuclear star formation and the molecular gas is discussed in § 5.1. In § 5.2 we conclude with a discussion of the importance of similar processes for the nuclear starbursts and the evolution of galactic nuclei. The results are summarized in § 6.

---

based on the luminosity of blue supergiants in 7 satellite galaxies (Karachentsev, Sharina, & Huchtmeier 2000), and  $5.7 \pm 0.7$  Mpc based on the expanding photo-spheres of Type II supernovae (Schmidt et al. 1994). Throughout this paper, we adopt the Tully (1988) value because it simplifies comparison to most other papers in the literature, and is consistent with the more recent estimates.

## 2. Observations and Data Reduction

### 2.1. The CO Data

The  $^{12}\text{CO}(1-0)$  and  $^{12}\text{CO}(2-1)$  lines at 3mm and 1mm, respectively, were simultaneously observed at two days in February 2002 using the IRAM Plateau de Bure interferometer (PdBI) with 6 antennas in its A and B configurations providing 30 baselines ranging in length from 30 to 400 m. The resulting uv coverage is shown in Fig. 1 and 2. The resulting resolution using uniform weighting<sup>3</sup> is  $1.25'' \times 1.01''$  (PA  $22^\circ$ ) and  $0.58'' \times 0.48''$  (PA  $-165^\circ$ ) for the  $^{12}\text{CO}(1-0)$  and  $^{12}\text{CO}(2-1)$  line, respectively. The calibration and mapping were done in the standard IRAM GILDAS software packages CLIC and MAPPING (Guilloteau & Lucas 2000). The phase center of the observations was at 20h34m52.36s +60d09m15.96s in the observed epoch of J2000.0. All velocities are observed relative to  $v_{\text{ref}}(\text{LSR}) = 65 \text{ km s}^{-1}$ . The integration times for NGC 6946 and the phase calibrator 2037+511 were divided into 20 and 3 scans with lengths of 60 and 45 seconds, respectively. During the observations the typical system temperature in the sideband containing the line of interest at 115 (230) GHz was about 270 (300–350) K.

For the bandpass, phase, and amplitude calibration we used observations of the quasar 2037+511 which was observed about every 20 minutes. The flux calibration was also checked on this source and resulted in an upper limit for the uncertainty in the flux calibration of about 10(17)% at 115(230) GHz. The pixel scales of the data cubes are  $0.2''/\text{pixel}$  and  $0.12''/\text{pixel}$  at 3mm and 1mm, respectively, with an image size of  $512 \times 512$  pixels to ensure that the dirty beam is well-sampled while all emission (even outside the primary beam) can be CLEANed. Channel maps were CLEANed with up to 1000 iterations down to a flux limit of  $1.5\sigma$ . In order for the CLEAN process to converge, we needed to define CLEAN regions. For the  $^{12}\text{CO}(1-0)$  data cube this was achieved using a 0th moment map derived from a CLEANed cube without any set CLEAN areas. Thus we defined the same CLEAN region for all channels. For the  $^{12}\text{CO}(2-1)$  data, it was necessary to separately define CLEAN regions for each individual channel. The correct choice of CLEAN regions was verified by inspecting the resulting residual maps for the presence of significant structure. The lack of missing information on very low spatial frequencies in the uv plane (i.e. very short baselines) is likely the main reason why a single region file was not applicable.

The spectral resolution during the observations was 1.25 MHz per channel both at 3mm and 1mm. The final rms in the binned  $6 \text{ km s}^{-1}$  wide channels is 4 and 12 mJy/beam for

---

<sup>3</sup>In the convention of the IRAM GILDAS package, uniform weighting corresponds roughly to a `robust=0` parameter in the AIPS package.

the  $^{12}\text{CO}(1-0)$  and  $^{12}\text{CO}(2-1)$  line, respectively, as measured in the channels where line emission is present. Using the equation to estimate the rms noise provided by IRAM<sup>4</sup> a theoretical rms of 3.5 and 8 mJy is expected for natural weighting under standard observing conditions and for our chosen bandwidth. Taking into account that we expect a higher rms due to the uniform weighting, the agreement between theoretical and actual rms is good.

The moment maps were calculated using the GIPSY task 'MOMENTS' requiring that emission is present above a certain clipping level in at least two adjacent channels. This minimizes the inclusion of noise peaks in the maps. We used a clipping level of  $3\sigma$  for the 0th moment (intensity map), and a  $4\sigma$  level for the 1st and 2nd moments (velocity field and dispersion map). We present the resulting channel maps of the  $^{12}\text{CO}(1-0)$  and  $^{12}\text{CO}(2-1)$  line emission in Fig. 1 and 2, respectively. Spectra extracted from the central  $4.8'' \times 4.8''$  are shown in Fig. 3. All data are presented without a primary beam correction applied.

## 2.2. Archival Data

In order to determine the missing flux in our data, we retrieved the  $^{12}\text{CO}(1-0)$  data of the BIMA SoNG project (Helfer et al. 2003) from NED. The data cube contains a combination of BIMA and 12m NRAO observations, and should contain the entire  $^{12}\text{CO}(1-0)$  flux, since the short spacings missed by the BIMA mm-interferometer are provided via the 12m single-dish data. The data cube has an angular resolution of  $6.0'' \times 4.9''$ , a channel width of  $10 \text{ km s}^{-1}$ , and an rms noise level of 61 mJy/beam (for details see Helfer et al. 2003). We calculated moment maps in a similar way to the PdBI data using a  $3\sigma$  cut-off for all three moments.

For comparison to our CO maps, we also obtained a number of optical and NIR images from various archives. For these, we used an H-band image from the 2MASS survey (Jarret et al. 2003) as a common reference frame by aligning field stars. We used the  $K_s$  band image of Knapen et al. (2003) to construct the gravitational potential for our qualitative dynamical model (see §4.3) of the inner stellar bar. In addition, we used the I-band continuum and  $\text{H}\alpha$  line emission images of Larsen & Richtler (1999) to compare the CO morphology to the large-scale star formation. For the modeling in §4.3, we also retrieved from the CDS archive the HI and  $\text{H}\alpha$  velocity curves from Carignan et al. (1990) and Blais-Ouellette et al. (2004), respectively.

Finally, we obtained higher resolution, space-based images from the *Hubble Space Tele-*

---

<sup>4</sup>e.g. [http://www.ram.fr/GENERAL/calls/calls\\_s06/node34.html](http://www.ram.fr/GENERAL/calls/calls_s06/node34.html)

*scope* (HST) archive for a more detailed comparison with the nuclear CO morphology: (i) an I-band image taken with WFPC2 in the F814W filter, (ii) a NICMOS H-band image, and (iii) a continuum-subtracted Pa $\alpha$  image. The latter two images were taken as part of the SINGS legacy project (HST-ID 9360, PI: R. Kennicutt). All HST images were also aligned to the 2MASS image using field stars. Given the resolution difference between ground- and space-based observations and the limited number of stars available for alignment, we estimate that our absolute astrometry of the HST images is good to within  $\sim 0.3''$  relative to the 2MASS image.

### 3. Observational Results

#### 3.1. CO Morphology: a Nuclear Gas Spiral

In Fig. 4, we present the intensity maps for both CO lines. The overall  $^{12}\text{CO}(1-0)$  morphology resembles that of the lower resolution maps (of  $\sim 4''$  and  $\sim 6''$ ) of the BIMA and NMA arrays (Regan & Vogel 1995; Helfer et al. 2003; Ishizuki et al. 1990). The two molecular arms extending to the north and south are clearly seen in the PdBI  $^{12}\text{CO}(1-0)$  intensity map. There is some evidence for multiple spiral arms, but whether this is a true  $m = 4$  spiral structure as claimed by Regan & Vogel (1995) is not obvious.

The molecular gas concentration in the inner  $15''$  (400 pc) could not be resolved with previous  $^{12}\text{CO}(1-0)$  observations: Ishizuki et al. (1990) proposed that it is a nuclear molecular bar based on its elongation and the presence of non-circular motions. On the other hand, Regan & Vogel (1995) concluded that the concentration is formed by the continuation of the outer (stellar) spiral arms. Recently, Meier & Turner (2004) suggested that the central concentration is actually a barely resolved ring which is fed via the outer northern and southern gas lanes which are produced by the large-scale bar.

Our new CO observations resolve for the first time the central molecular gas concentration into a S-shaped spiral with an extent of about  $10''$  (270 pc). For the remainder of this paper, we will use the term “nuclear spiral” to describe this feature. The higher-resolution  $^{12}\text{CO}(2-1)$  map (Fig. 4b) shows in detail how the molecular gas is distributed within the nuclear spiral. The gas is concentrated in three bright clumps (indicated in Fig. 5), one on either side of the nucleus at a radial distance of  $\sim 4''$  or 120 pc, and a third clump that coincides with the dynamical center, at least within the uncertainty of our astrometry (see § 3.3).

Overall, the morphology of the nuclear gas spiral closely resembles a scaled-down version of the gas flow in a large-scale stellar bar predicted by dynamical models (e.g. Athanassoula

1992). The two outer clumps are connected to the nuclear one via straight gas lanes which run along a position angle of  $PA \sim -40^\circ$ . Both gas lanes are offset from each other by about  $2''$  perpendicular to their length. Also, the three clumps are extended perpendicularly to the length of the gas lanes. In § 4.3, we will show that the nuclear spiral can indeed be well explained by the gas responding to the gravitational potential of the small inner stellar bar in the center of NGC 6946.

### 3.2. CO Kinematics: Radial Gas Inflow

Overall, the  $^{12}\text{CO}(1-0)$  velocity field (Fig. 6a) exhibits a well-defined pattern. The dominant motion is from North-East to South-West, in agreement with a position angle  $PA \sim 242^\circ$  of the kinematic major axis derived from HI observations (Crosthwaite 2002). One prominent exception is the gas in the northern gas lane which seems to move from East to West. The zero velocity curve reveals several changes (or wiggles) in the region of the nuclear spiral structure. The changes are closely associated with the spiral structure as is clearly seen in the  $^{12}\text{CO}(2-1)$  data (Fig. 6b). Along the inner ridge of the southern clump the velocity of the gas is blue-shifted with respect to the systemic velocity, whereas it appears red-shifted along the inner ridge of the northern clump. Assuming that the spiral arms are trailing, the northeastern side of NGC 6946 is the near side. This is consistent with the high extinction northeast of the nucleus that is apparent in optical and NIR images which is expected to occur on the near side of galaxies (de Vaucouleurs 1958). The observed velocities therefore suggest that the molecular gas motion has a radial component towards the nuclear clump. Inside the nuclear clump ( $r \leq 2''$ ), the position angle of the major kinematic axis is closer to an east-west orientation. All this indicates the presence of strong non-circular gas motions, most likely inwards streaming onto the nuclear clump which reduces the apparent circular velocity at a given radius.

The position-velocity (p-v) diagrams (Fig. 7) along the major and minor kinematic axes of  $242^\circ$  and  $152^\circ$  (Crosthwaite 2002) can be used to derive additional kinematic and geometric properties of the nuclear gas clump itself, i.e. inside 30 pc from the kinematic center:

*First*, there are two peaks in the steep part of the p-v diagrams along the major kinematic axis at  $r \sim 0.45''$  (Fig. 7a,c) which suggests that the nuclear clump is not a smooth disk, but rather has a hole inside, i.e. is ring-like. Sakamoto et al. (1999) called this a “hole feature” in the case of a steeply rising rotation curve with circular motion only (see their appendix A for a detailed discussion). Alternatively, such a feature could be caused by Keplerian motion due to a central black hole or higher velocity dispersion in the center. The second scenario is likely not the case for NGC 6946, as velocity dispersion map shows no such increase towards

the dynamical center (see below). In addition, two peaks are also seen along the minor axis (Fig. 7b,d) at  $r \sim 0.33''$ . The spatial offsets indicate a radius for this ring-like distribution (hereafter: nuclear ring) of about  $r_{\text{ring}} \approx (9 - 13)$  pc when taking inclination into account. It is interesting to note that a third peak is present in the  $^{12}\text{CO}(2 - 1)$  p-v diagram which is not seen in the  $^{12}\text{CO}(1 - 0)$  one. This might be either due to angular resolution effects or it might indicate real variations in the line ratios of the molecular gas in this putative nuclear ring.

*Second*, as already noted by several authors (Ishizuki et al. 1990; Regan & Vogel 1995; Meier & Turner 2004), the non-zero velocity along the minor axis strongly suggests streaming motions in the central 300 pc. Our new CO data allow us to trace this non-zero component well inside the nuclear clump. Inside a radius of  $\sim 1''$  (see Fig. 7d) and coincident with the location of the nuclear ring at a radius of  $r \sim 0.45''$ , the gas changes the sign of its velocity along the minor axis suggesting that strong streaming motion are associated with this nuclear ring at a distance of only about 11 pc. It is not clear, if this non-circular motion could be only mimicking the presence of a ring-like structure. However, the twin-peaked structure of the central clump suggests that a true depression is present.

*Third*, the nuclear flux distribution appears to be asymmetric with respect to the observed reference velocity. The p-v diagrams in Fig. 7 are plotted relative to the reference velocity of our PdBI observations which was set to  $v_{ref}(LSR) = 65 \text{ km s}^{-1}$ , based on the CO p-v diagram in Fig. 4 of Sakamoto et al. (1999). The obvious offset of the p-v structure with respect to zero velocity then indicates that the gas in the nuclear ring moves with about  $-25 \text{ km s}^{-1}$  relative to the reference velocity implying a systemic velocity of  $v_{\text{sys}}(LSR) \approx 40 \text{ km s}^{-1}$ . However, a slightly higher value of  $v_{\text{sys}}(LSR) \approx 50 \text{ km s}^{-1}$  (indicated by the horizontal line in the p-v diagrams of Fig. 7) for the systemic velocity is suggested when taking into account the motion of the bulk of the emission. A systemic velocity of  $v_{\text{sys}}(LSR) = 50 \text{ km s}^{-1}$  has also been suggested by several authors based on the extended atomic gas emission (e.g. Carignan et al. 1990; Crosthwaite 2002). Thus, we are led to conclude that the nuclear flux distribution is not symmetric with respect to the systemic velocity and has an offset relative to  $v_{\text{sys}}$  by about  $-15 \text{ km s}^{-1}$ .

The velocity dispersion in the disk outside the nuclear spiral structure is generally below  $10 \text{ km s}^{-1}$  in both CO lines. The  $^{12}\text{CO}(1 - 0)$  dispersion map (Fig. 8a) shows values between about 25 and  $35 \text{ km s}^{-1}$  inside the spiral structure, whereas the derived velocity dispersion in the  $^{12}\text{CO}(2 - 1)$  map (Fig. 8b) is about  $5 \text{ km s}^{-1}$  lower. This difference is very likely due to the higher spatial resolution of the  $^{12}\text{CO}(2 - 1)$  data which reduces beam smearing effects. One interesting aspect is that the velocity dispersion seems to increase when crossing the southeastern gas lane from the leading to the trailing side, i.e. from northeast to southwest.

A similar pattern is only barely indicated for the northwestern gas lane. Such a behavior is expected when streaming motions due to a stellar bar are present. This will be further explored in §4.3.

The velocity dispersion inside the nuclear clump is about  $10 - 20 \text{ km s}^{-1}$  higher than throughout the nuclear spiral. The dispersion reaches a maximum of about 50 and  $42 \text{ km s}^{-1}$  in the  $^{12}\text{CO}(1-0)$  and  $^{12}\text{CO}(2-1)$  line, respectively. This dispersion peak is slightly offset – as already expected from the p-v diagrams – from both the intensity peak and the dynamical center (see §3.3). Given our angular resolution of  $0.6''$ , it is difficult to decide how much of this offset is an artifact produced by beam smearing effects.

### 3.3. The Dynamical Center and the CO Rotation Curve

We used two approaches to derive a rotation curve from our  $^{12}\text{CO}(1-0)$  and  $^{12}\text{CO}(2-1)$  data: a) an automated fit to the velocity fields using the GIPSY task 'ROTCUR', and b) interactive fitting of the 3-dimensional data-cube using the GIPSY task 'INSPECTOR'. Both tasks are based on the assumption that the gas motions can be described by a model of rotating tilted rings. In principle, the inclination, position angle, center, and systemic and circular velocity of the individual rings are free parameters. In order to constrain this large parameter space, we fixed the inclination and the position angle of the rings to the values found for the large-scale HI disk of  $i \sim 38^\circ$  and  $PA \sim 242^\circ$  (Carignan et al. 1990; Crosthwaite 2002). We assume that these describe best the parameters of the galactic disk in NGC 6946 and that the central CO emission is in the plane of the galaxy.

The dynamical center was determined from the  $^{12}\text{CO}(2-1)$  p-v diagrams in Fig. 7 as the position which maximizes the symmetry of the velocity structure relative to the systemic velocity. As discussed in §3.2, we adopt a systemic velocity of  $v_{sys}(LSR) = 50 \text{ km s}^{-1}$  (i.e.  $15 \text{ km s}^{-1}$  lower than the reference velocity of the observations). This approach yields the following coordinates for the dynamical center: R.A.: 20h34m52.355s, Dec.: +60d09m14.58s (J2000). We estimate the uncertainty of our dynamical center position to be  $\sim 0.3''$ , dominated by the rather complex velocity structure in the central  $< 1''$ . Within this uncertainty, our coordinates agree well with those measured by Meier & Turner (2004), see also Fig. 9.

After “freezing” the dynamical center to the above coordinates, the final rotation curves were obtained with only the circular velocity as a free parameter. The derived (deprojected) rotation curves for the  $^{12}\text{CO}(1-0)$  and  $^{12}\text{CO}(2-1)$  line all show a steep rise at small radii and then level off at about  $125 \text{ km s}^{-1}$  (Fig. 10). The steeper gradient of the  $^{12}\text{CO}(2-1)$  rotation curve at  $r < 6''$  is expected because of the higher angular resolution of these line

data. The rotation curves obtained with the 'INSPECTOR' task are, in general, steeper than the ones produced with the 'ROTCUR' task. This is also expected because they result from direct fits to the 3-dimensional data cubes, and are therefore less affected by beam smearing (Swaters 1999).

In order to test whether the drop of the PdBI CO rotation curves beyond a radius of  $\sim 10''$  is real or an artifact due to the sampling of our data, we used the BIMA SoNG  $^{12}\text{CO}(1-0)$  data which have lower angular resolution ( $\sim 6''$ ), but cover a wider field. The BIMA SoNG rotation curve over-plotted in Fig. 10 was derived using 'ROTCUR' with the same parameter set as for the PdBI data. As expected from the larger BIMA beam, it shows an inner rise which is shallower. At larger radii, the rotation curve stays flat out to  $75''$ . The apparent drop for  $r > 4''$  ( $r > 9''$ ) seen in the PdBI  $^{12}\text{CO}(2-1)$  ( $^{12}\text{CO}(1-0)$ ) curves produced with 'ROTCUR' is an artifact produced by a lack of spatial coverage in our data, emphasized by the fact that 'ROTCUR' uses only 2-dimensional velocity fields instead of the full data cube. Our CO rotation curves are consistent with that of Meier & Turner (2004) once beam smearing effects are taken into account.

### 3.4. Molecular Gas and Dynamical Mass

The amount of molecular gas contained within the central few hundred parsec provides a gauge for the efficiency and sustainability of the current nuclear star formation activity. In order to estimate the molecular gas mass, we have calculated (after correcting for the primary beam response) the  $^{12}\text{CO}(1-0)$  flux contained in five distinct apertures in the center of NGC 6946: i) the central  $50''$ , i.e. the area containing the entire  $^{12}\text{CO}(1-0)$  emission in Fig. 4a, ii) the nuclear spiral, i.e the entire area of Fig. 4b, and iii) the three bright CO clumps within the nuclear spiral that are marked in Fig. 5. The results are summarized in Table 1.

The total flux contained in the  $^{12}\text{CO}(1-0)$  map of Fig. 4a is about 50% of that measured over the same area in the short spacing-corrected BIMA SoNG data (see Tab. 1). This means that about half the emission stems from an extended component which is not sampled by the PdBI baselines. As for components ii) and iii), missing flux is less of a concern because their spatial extent is well-matched to the angular scales probed by the PdBI observations.

In order to convert the measured CO flux into a molecular gas mass for the individual components (see Tab. 1), we used  $M_{\text{H}_2}[\text{M}_\odot] = \frac{S_{\text{CO}} \times c^2}{2k\nu^2} X_{\text{CO}} \times D^2 \times 2m_p = 519295 \times S_{\text{CO}}[\text{Jy km s}^{-1}]D[\text{Mpc}]^2 X_{\text{CO}}/\nu[\text{Hz}]^2$  (e.g. Braine et al. 2001) with the Distance D, speed of light c, Boltzmann constant k, and the proton mass  $m_p$ . We assumed a  $X_{\text{CO}}$  conversion

factor of  $X_{\text{CO}} = 2 \times 10^{20} \text{cm}^{-2} (\text{K km s}^{-1})^{-1}$  (Strong et al. 1988) and an observed frequency of  $\nu = 115.246 \text{ GHz}$ . This results in a molecular gas mass of  $3.1 \times 10^8 M_{\odot}$  contained in the entire map, and  $9.3 \times 10^7 M_{\odot}$  within the nuclear spiral. About 1/6 of this latter mass is located within the nuclear clump which has a size of about  $2'' \times 1.5''$  ( $\approx 60 \text{ pc} \times 45 \text{ pc}$ ). The northern clump is about half as massive as the nuclear clump, while the southern clump contains about 50% more molecular gas. Note, however, that the value of the  $X_{\text{CO}}$  conversion factor in the center of NGC 6946 has been estimated to be 4-5 times lower than the standard value (Meier & Turner 2004; Walsh et al. 2002). The gas masses listed in Table 1 could therefore be overestimated by this factor.

Assuming that solid body rotation is a reasonable approximation for the gas dynamics in the central  $4''$ , we can estimate the dynamical mass contained in the inner 110 pc. From the  $^{12}\text{CO}(2-1)$  rotation curve (Fig. 10), we find a rotational velocity of  $v \approx 155 \text{ km s}^{-1}$  at a radius of  $r = 2''$  ( $\approx 55 \text{ pc}$ ) which translates into a dynamical mass of  $M_{\text{dyn}} \sim 3.1 \times 10^8 M_{\odot}$ . For comparison, Engelbracht et al. (1996) give a  $2\sigma$  upper limit on the dynamical mass of  $M_{\text{dyn}} \sim 3 \times 10^8 M_{\odot}$  inside a radius of  $4.25''$  ( $\approx 115 \text{ pc}$ ) based on the velocity dispersion of stellar absorption lines as measured from long slit NIR spectra with  $R \approx 3000$ .

After accounting for the contribution of He (36%) to the total gas mass, the mass in the central  $4''$  of  $\sim 3.1 \times 10^7 M_{\odot}$  is between about 2% (for the lower limit in the  $X_{\text{CO}}$  conversion factor) and 10% of the enclosed dynamical mass. This value is in reasonable agreement with the molecular gas fraction of  $\sim 5\%$  for the inner  $6''$  found by Meier & Turner (2004). Therefore, the molecular gas fraction in the center of NGC 6946 appears to be similar to the molecular gas fraction observed in the central kiloparsec of nearby spiral galaxies (Sakamoto et al. 1999; Sheth et al. 2005).

## 4. What Drives the Gas Flow?

### 4.1. The Large Scale

The classification of dynamical modes in NGC 6946 is hampered by the fact that the spiral structure is complex and can not be easily classified. Elmegreen et al. (1992) find evidence for a superposition of  $m = 2$  and  $m = 3$  modes. From the analysis of a combined HI and CO (residual) velocity field, Crosthwaite (2002) also finds evidence for an outer  $m = 3$  and an inner  $m = 2$  mode. Both modes appear to have the same pattern speed. The derived corotation radius is at  $(4.5 \pm 0.5)'$  or  $\approx (7.3 \pm 0.8) \text{ kpc}$ .

NGC 6946 is classified as a barred spiral both in the RC3 catalog and LEDA (de Vaucouleurs et al. 1992; Paturel et al. 2003). The length of the large-scale bar or oval was first

reported by Regan & Vogel (1995) to be about  $120''$  ( $\approx 3.3$  kpc), well inside the corotation radius of the spiral structure (see also Elmegreen et al. 1998). Recently, Menéndez-Delmestre et al. (2006) have confirmed this length from 2MASS images, and give a position angle of  $\sim 17^\circ$  for the bar. The flat abundance gradient throughout the central 5 kpc of NGC 6946 reported by Belley & Roy (1992) could be explained in the context of the presence of a bar, which is expected to enhance radial mixing.

However, the large-scale bar appears to leave no obvious signature in the observed gas kinematics, which might not come as a surprise given its low ellipticity of 0.15 (Elmegreen et al. 1998). The BIMA SoNG observations (Helfer et al. 2003), which cover most of the area of the large-scale bar, show a concentration of molecular gas in the inner  $0.5'$ , with some hints of gas lanes extending toward the north and south. The higher resolution PdBI observations of the  $^{12}\text{CO}(1-0)$  line resolve the inner gas concentration, but there is no obvious pattern which can readily be associated with this large-scale bar. On the other hand, the comparison between the  $^{12}\text{CO}(1-0)$  intensity distribution and the  $\text{H}\alpha$  line emission in the inner arcminute is not inconsistent with gas responding to a stellar bar. As can be seen in Fig. 11, the  $\text{H}\alpha$  emission is strongest on the leading side of the CO lanes, especially on the northern side. This spatial correlation between molecular gas and current star formation seems fairly typical as it is observed for many large-scale stellar bars (Sheth et al. 2002).

Nevertheless, we conclude that the details of the **nuclear** gas distribution and kinematics studied in this paper are likely not affected by the presence of the large-scale bar, and we will therefore ignore its presence for our modeling efforts described in § 4.3.

## 4.2. The Inner NIR Bar

NGC 6946 is known to host a small-scale stellar bar (Regan & Vogel 1995) which has been studied in more detail by Elmegreen et al. (1998). In Fig. 12, we compare the NIR morphology from the  $K_s$  band image of Knapen et al. (2003) to the  $^{12}\text{CO}(2-1)$  distribution in the central kpc of NGC 6946. The apparent diameter of the inner bar has been estimated by Elmegreen et al. (1998) from ellipse fitting to be  $\sim 8''$  with an ellipticity of 0.4 and a position angle of about  $140^\circ$ . Deriving the exact length of the inner bar is not straightforward in the case of NGC 6946, as large extinction is present in the inner kpc (see § 5.1).

Therefore, the  $8''$  length of the inner bar reported by Elmegreen et al. (1998) should probably be regarded as a lower limit. This is supported by Fig. 12 which compares the observed isophotes of the  $K_s$  band emission with (theoretical) circular isophotes of  $5''$ ,  $10''$ , and  $15''$  radius projected into the galaxy plane: only the outermost  $K_s$  isophote with a radius

of  $15''$  appears close to being circular. For smaller radii, the deviation from axisymmetry is still high, strongly suggesting that the NIR bar is more extended than the  $\sim 8''$  diameter reported by Elmegreen et al. (1998). A larger NIR bar size is also supported by gas dynamical models which show that gas lanes always form inside the bar potential (e.g. Athanassoula 1992). Assuming an ellipticity of 0.4 for the inner bar (Elmegreen et al. 1998), its apparent length should therefore be  $\sim 16''$  (i.e. twice as large as measured by Elmegreen et al. 1998) in order to encompass the gas lanes.

As shown in §3.1, the morphology of the CO spiral in NGC 6946 is remarkably reminiscent of gas lanes in a barred potential. Such a distribution can only be stationary, if either (a) the rotation is rigid in the central few arcseconds over the extent of the structure or (b) it is a density wave (caused by e.g. the NIR bar). As the velocity is not linearly increasing with radius outside a radius of  $\sim 3.5''$  (see Fig. 10), this leaves only a density wave as the cause for the spiral structure unless the spiral is observed at a special time.

As already described in §3.2, the velocity field shows various signatures expected for gas moving in a barred potential. The iso-velocity lines are twisted away from the kinematic minor axis in the region of the inner NIR bar. There is also an abrupt change in the orientation of the iso-velocity contours in the innermost  $2''$ , with the zero velocity curve almost along a North-South direction. Such a behavior is expected in the presence of an Inner Lindblad Resonance (ILR) where the outer  $x_1$  orbits elongated along the bar major axis are replaced by  $x_2$  orbits inside the ILR which are elongated along the bar minor axis (e.g. Athanassoula 1992).

Figure 13 shows four representative p-v diagrams along cuts that run perpendicular to the northern and southern gas lanes (see Fig. 9 for the exact location of the p-v cuts). An abrupt change in velocity is apparent in the southern p-v diagrams, and - less prominently - also in the northern ones. Such a jump in velocity is expected to occur as the gas enters the shock region inside the gas lane (see for comparison Fig. 11 in Athanassoula 1992).

The qualitative arguments presented in this section suggest that the observed CO morphology and kinematics can be explained by the gas responding to a barred potential. We now proceed to the next level of detail, and construct a simple dynamical model of NGC 6946 in an attempt to qualitatively reproduce the observed central CO distribution and kinematics in the context of gas flows within an inner small bar.

### 4.3. Modeling the Central Kiloparsec

Our modeling efforts follow the formalism used in Emsellem, Goudfrooij, & Ferruit (2003), (see also Wada & Koda 2001): an initial axisymmetric mass model is perturbed via the addition of a bar-like structure, and gas orbits are then derived from a treatment of the epicycle approximation including a damping term.

The first step in creating an axisymmetric mass model is to obtain a three-dimensional, axisymmetric *luminosity* model which reasonably approximates the observed photometry. For this purpose, we use the  $K_s$  band image of NGC 6946 obtained by Knapen et al. (2003). We first deproject the  $K_s$  band image assuming that the galaxy is two-dimensional with its major axis at a position angle of  $PA = 242^\circ$  and an inclination of  $i = 38^\circ$ . We then obtain an analytical face-on model by simply fitting the resulting deprojected image with a Multi-Gaussian-Expansion model (Monnet et al. 1992; Emsellem et al. 1994, MGE hereafter) constraining all components to be circular (i.e. an axis ratio equal to 1) and taking into account a Gaussian point spread function of  $FWHM = 1''$  to account for atmospheric seeing. The resulting MGE model is arbitrarily thickened with an axis ratio varying continuously from 0.25 in the outer part to 0.8 in the central  $2''$ . Figure 14 compares this model after projection (using again the assumed inclination of  $38^\circ$ ) with the original  $K_s$  band image. The fit is reasonably good considering the imposed constraint of axisymmetry. The vertical height of the luminosity distribution is rather unconstrained, and our model is obviously not designed to reproduce the large-scale stellar bar and the spiral structure. It will therefore only serve, as mentioned above, as a reference model for the inner few arcseconds of the galaxy in order to probe the potential role of the inner tumbling bar potential. We have, however, checked that the results described below are not significantly influenced by, e.g., a change in the vertical height. In the following, we also assume that the large-scale bar does not play any major role in the central  $10''$ , as discussed in § 4.1.

The knowledge of the spatial luminosity distribution allows us to derive the corresponding axisymmetric gravitational potential by simply using Poisson equation and assuming a constant mass-to-light ratio  $M/L_{K_s}$  in the  $K_s$  band. We constrain  $M/L_{K_s}$  by comparing the predicted circular rotation curve  $V_c(r)$  in the equatorial plane with the observed deprojected HI and  $H\alpha$  rotation curves (Fig. 15) obtained by Carignan et al. (1990) and Blais-Ouellette et al. (2004), respectively: we obtain  $M/L_{K_s} = (0.72 \pm 0.1)$ , a value adopted for the rest of this Section.

We then add a bar-like perturbation  $\delta\Phi$  to the axisymmetric gravitational MGE potential in the form described in Emsellem et al. (2003), with  $\delta\Phi = \Phi_2 \times \cos(2\theta)$ . This component corresponds to the small-scale inner NIR bar. We assume for this bar component the same  $M/L_{K_s}$  ratio as for the stars in the outer galactic disk, although this may be an

overestimate considering the presence of young stars in the central region. Gaseous orbits are then derived via the linear epicycle approximation, and including an artificially induced damping (simulating the dissipative nature of the gas) described by a parameter  $\Lambda$  [ $\text{km}^2 \text{s}^{-2}$ ]. The radius, force and pattern speed of the bar are provided by  $R_{bar}$  [ $''$ ],  $Q_{bar}$  [ $\text{km}^2 \text{s}^{-2}$ ], the amplitude of the perturbation, and  $\Omega_p$  [ $\text{km s}^{-1} \text{kpc}^{-1}$ ], respectively. The bar radius  $R_{bar}$  corresponds to the radius where the contribution from the bar component is designed to drop (as  $r^{-4}$ ).

In order to constrain some of these parameters, we assume that the bar encompasses the southern and northern clump: this implies that the radius of the bar is  $R_{bar} > 5''$ , and imposes an upper limit on its pattern speed  $\Omega_p \sim 1100 \text{ km s}^{-1} \text{kpc}^{-1}$ , so that the bar lies within its corotation radius. We have derived models for  $5'' \leq R_{bar} \leq 10''$  and  $100 \text{ km s}^{-1} \text{kpc}^{-1} \leq \Omega_p \leq 1100 \text{ km s}^{-1} \text{kpc}^{-1}$ , with the aim to qualitatively reproduce the observed distribution and kinematics of the  $^{12}\text{CO}(1-0)$  line emission in the central  $10''$ . For each model, we compute the observed density distribution and first two velocity moments, the velocity field and the dispersion map. The predicted maps are derived by first assuming an initially unperturbed radial density distribution for the gas, and take into account the resolution of the  $^{12}\text{CO}(1-0)$  data with a clean beam size of  $1.12''$ . Only models with  $6.5'' \leq R_{bar} \leq 8''$  and  $510 \text{ km s}^{-1} \text{kpc}^{-1} \leq \Omega_p \leq 680 \text{ km s}^{-1} \text{kpc}^{-1}$  can roughly reproduce the length and shape of the  $^{12}\text{CO}(1-0)$  gas lanes. It is however difficult to further constrain these parameters given the observed patchiness in the distribution of the  $^{12}\text{CO}(1-0)$  line emission, and the asymmetry of its velocity field. The derived range of bar lengths of  $13''$  to  $16''$  is consistent with the inferred range of observed apparent bar length of about  $8'' < l_{bar,obs} < 30''$  (when correcting for inclination:  $10'' < l_{bar} < 38''$ ; see §4.2).

A comparison between a representative model and the data is shown in Fig. 16. The model parameters were  $\Lambda = 1800 \text{ km}^2 \text{s}^{-2}$ ,  $R_{bar} = 7.5''$ ,  $Q_{bar} = (350)^2 \text{ km}^2 \text{s}^{-2}$  and  $\Omega_p = 510 \text{ km s}^{-1} \text{kpc}^{-1}$ . The corresponding corotation radius is then at  $\sim 9.5''$  ( $\sim 260 \text{ pc}$ ), and the southern and northern clumps are close to the Ultra Harmonic 4:1 Resonance (UHR) at  $6.7''$ . This model reproduces the extent and position angle of the observed straight gaseous lanes which end near the UHR with an abrupt change in the pitch angle: such a structure resembles the one observed in the ionized gaseous inner component in the early-type galaxy NGC 2974 (Emsellem et al. 2003), also interpreted in the context of an inner tumbling bar. In the present model, the corresponding ILR lies then at  $\sim 2.2''$ , just outside the extent of the nuclear clump.

The predicted velocity field exhibits clear deviations from circular motions: this is best illustrated by the wiggles in the zero velocity isovelocity line which significantly departs from the kinematic minor axis, with a peak difference of about  $30^\circ$  along the gas lanes. At a radius

of about  $5''$ , the zero velocity curve gets back to the kinematic minor axis, a feature clearly present in the  $^{12}\text{CO}(1-0)$  velocity field of NGC 6946: this may be interpreted in the model as a change in the orbital structure near the UHR of the bar component. The velocity twist in the central  $2''$  of the model is however not strong enough to reproduce the one observed in the  $^{12}\text{CO}(1-0)$  velocity field. Overall, the predicted velocities are too high by about 20%: as mentioned above, this may indicate that  $M/L_{K_s}$  is lower in the central 500 pc than in the outer part of the disk due to the presence of young stars.

The crowding of orbits near the gas lanes also implies strong shocks and high velocity dispersion values. The  $^{12}\text{CO}(1-0)$  maps of NGC 6946 indeed hint at the presence of such high dispersion values located on the inner (trailing) side of the gas lanes. The exact locations of the high dispersion regions along the gas lanes relative to the densest regions strongly depend on the prescription for the shocks (damping), which are clearly not properly addressed with the present static model. In this model, high central dispersion values are indeed mostly due to orbit crowding and unresolved velocity broadening, i.e. beam smearing effects. A more realistic physical treatment of the shock regions would require full hydro-dynamical simulations.

The NIR isophotes and the  $^{12}\text{CO}(1-0)$  kinematics in the central  $10''$  of NGC 6946 exhibit signatures of a stellar bar (see §4.2). Although the model shown here (Fig. 16) is clearly not meant as a fit to the data, it illustrates that the observed gas distribution and kinematics are indeed qualitatively consistent with the presence of an inner stellar bar of about 200 pc radius. Such a bar would thus naturally explain:

- the presence of straight gas lanes, on the leading edge of the bar, which are then regions of shocks located roughly between the ILR and UHR.
- the abrupt change in the gas density distribution near the UHR, a feature also observed in more realistic hydro-dynamical simulations, such as the one performed by Maciejewski et al. (2002), and
- the associated strong twist of the iso-velocities near the end of the gas lanes.

In this context, the gas concentration in the central clump could be interpreted as the result of gas accumulation within the ILR of the inner bar. Models such as the one described in Maciejewski et al. (2002), indicate that such gas could settle on a nuclear ring: this would also be consistent with the ring-like morphology of the nuclear clump as inferred from its  $^{12}\text{CO}(2-1)$  p-v diagrams (see §3.2). The high central gas density, as well as the presence of shocks in the inner 150 pc, are likely necessary ingredients for the high star formation

efficiency in the center of NGC 6946. More realistic hydro-dynamical simulations, possibly in combination with higher resolution maps of the molecular gas, are required to confirm these results, and to further constrain the mechanisms that cause the nuclear starburst in NGC 6946.

It is interesting to compare the case of NGC 6946 to that of the early-type galaxy NGC 2974. The CO distribution observed in NGC 6946 is strikingly similar to the ionized gas structure revealed by WFPC2 narrow band images of NGC 2974 (Emsellem et al. 2003) which reveal straight gas lanes and the presence of a central gaseous concentration within the inner 10 pc. These features were interpreted in NGC 2974 as being driven by an inner bar with a diameter of  $\sim 540$  pc and a pattern speed around  $700 \text{ km s}^{-1} \text{ kpc}^{-1}$ , values comparable to the ones derived for the inner bar of NGC 6946. The main difference then lies in the overall low dust and gas content ( $\sim 6.8 \times 10^4 M_{\odot}$  of ionized gas) and the absence of significant star formation in NGC 2974, as expected for its E/S0 classification. The inner bar of NGC 2974 may therefore represent an early-type analog of the one in NGC 6946, the gas reservoir of NGC 2974 not being sufficient to have triggered a significant starburst. In both cases, however, the dynamical time-scale is similarly short ( $\sim 10^6$  yr at about 200 pc from the center), which implies a strongly time-varying gaseous distribution.

## 5. Discussion

### 5.1. The Central Starburst

The central 300 pc ( $\sim 11''$ ) of NGC 6946 currently experiences intense star formation. This is evident from the multitude of hydrogen recombination lines in the spectrum of its nuclear region (see e.g. Engelbracht et al. 1996), but also by the morphology of the Pa $\alpha$  emission in the *HST/NICMOS* image shown in Fig. 17. It is thus not surprising that NGC 6946 is classified to have an HII region nucleus based on the [OI]/H $\alpha$  and [SI]/H $\alpha$  line ratios (Ho, Filippenko & Sargent 1997).

In order to estimate the current star formation rate (SFR) in the nucleus of NGC 6946, we have measured the Pa $\alpha$  flux of the central  $8''$  from the image of Böker et al. (1999a) which is  $5.5 \times 10^{-13} \text{ erg s}^{-1} \text{ cm}^{-2}$ . We assume for the moment an average extinction of  $A_V = 4.6$  mag as derived for the southern “hot spot” in Fig. 17 by Quillen & Yukita (2001) from estimates of the H $\alpha$ /Pa $\alpha$  line ratio. Then applying the extinction law of Cardelli et al. (1989) with  $R_V = 3.1$ , and assuming an intrinsic H $\alpha$ /Pa $\alpha$  line ratio of 7.41 (appropriate for case B recombination with  $T_e = 5000$  K and  $N_e = 100 \text{ cm}^{-2}$ , see Osterbrock 1989), we can derive an intrinsic H $\alpha$  flux of  $7.6 \times 10^{-12} \text{ erg s}^{-1} \text{ cm}^{-2}$ . Converting to H $\alpha$  luminosity (with

$D = 5.5$  Mpc) and applying the relation of Kennicutt (1983), this translates into a current SFR of  $0.25 M_{\odot} \text{ yr}^{-1}$ .

However, this simple calculation most likely leads to an underestimate of the true SFR due to the large extinction present in the nucleus of NGC 6946. The fact that the extinction in the center of NGC 6946 is rather high and uneven is apparent from the HST I-band image in Fig. 17. The stellar continuum emission is rather asymmetric, and noticeably reduced in regions of high gas density. It is also apparent from the J-K color map in Fig. 10 of Elmegreen et al. (1998) which shows a remarkable similarity to the CO distribution demonstrating that the dust associated with the molecular gas causes significant extinction. It is clear from Fig. 17 that both line and continuum emission are significantly suppressed in regions of high gas density, i.e. the CO spiral and especially the three clumps marked in Fig. 5.

One aspect of uncertainty is the geometry of the obscuring dust. For example, Engelbracht et al. (1996) derive an extinction of  $A_V \sim 10.4$  for the central  $8.5''$  based on emission lines assuming that stars and dust are mixed. For comparison, they infer  $A_V \sim 4.3$  assuming a screen geometry for the dust, which agrees well with the Quillen & Yukita (2001) value. An alternative approach to obtain an extinction estimate for these regions which are basically opaque for recombination lines is to use the molecular gas surface density. For example, assuming that the molecular gas in the nuclear clump is uniformly distributed over its area, we obtain an  $\text{H}_2$  surface mass density of  $M_{\text{H}_2}/A = 1.6 \times 10^7 M_{\odot}/(\pi \times (27 \text{ pc})^2) \approx 7000 M_{\odot} \text{ pc}^{-2}$ . This corresponds to an  $\text{H}_2$  column density of  $N(\text{H}_2) \approx 4.4 \times 10^{23} \text{ cm}^{-2}$ . Adopting the Galactic extinction relation of  $A_V/N_{\text{H}} = 6 \times 10^{-22} \text{ cm}^2 \text{ mag}$  (Draine 2003), we derive an extinction in the optical of  $A_V = 6 \times 10^{-22} \times 2N(\text{H}_2) = 528 \text{ mag}$ . Even taking into account the uncertainty in the  $X_{\text{CO}}$  conversion factor discussed in §3.4 which could lead to extinction values that are lower by a factor of 4-5, it is clear that the *average* extinction across the central  $\approx 60$  pc is most likely higher than the values derived by Engelbracht et al. (1996) and Quillen & Yukita (2001). This in turn implies that the true SFR is likely higher than the  $0.25 M_{\odot} \text{ yr}^{-1}$  value derived above. Observations in the mid-infrared would be required to solve this large discrepancy.

From the high  $\text{H}_2$  surface density across the nuclear gas clump, we conclude that the true nucleus of NGC 6946 is highly obscured even at NIR wavelengths. It is thus possible that the two bright  $\text{Pa}\alpha$  peaks on either side of the dynamical center (Fig. 17) are merely an artifact caused by the high extinction of the central CO clump. If, however, the peaks are true “hot spots” and their  $\text{Pa}\alpha$  emission is indeed produced by photoionization regions around young stars (as opposed to shocks resulting from a possible outflow from the nucleus), it is interesting to point out that their location roughly coincides with the ILR inferred from the dynamical model in §4.3. We thus might be observing a small-scale analog to the

kiloparsec-scale starburst rings seen in many barred spirals.

Finally, we point out that the active star formation as traced by the Pa $\alpha$  emission is, in general, not well correlated with the molecular gas. While for very young starbursts, this is a consequence of the gas shroud obscuring the view into the starburst, once massive stars have formed, their intense UV-radiation, stellar winds, and supernova explosions all combine to photo-dissociate and/or expel the CO gas. As a consequence, it is highly unlikely to observe both dense molecular gas, and signatures of active star formation in the same location.

## 5.2. Is the Center of NGC 6946 Peculiar?

It is interesting to compare the properties of the inner few hundred parsecs in NGC 6946 to those of similar late type spiral galaxies such as our Galaxy or IC 342. Although NGC 6946 is of somewhat later Hubble type (Scd vs. Sbc) and slightly less luminous ( $M_V = -19.1$  vs.  $M_V = -20.6$ ) than the Milky Way, in many respects both galaxies turn out to be fairly similar. For example, the dynamical mass within the inner  $\sim 110$  pc is nearly identical in both galaxies:  $\sim 3.1 \times 10^8 M_\odot$  for NGC 6946 (see § 3.4) and  $\sim 3.5 \times 10^8 M_\odot$  for the Galactic Center (derived from Fig. 7.1 in Genzel et al. 1994). Moreover, the distribution and kinematics of the molecular gas appear similar in both galaxies. This can be seen by comparison with the recent study of Sawada et al. (2004) who derived the face-on geometry of the molecular gas in the central kiloparsec of the Milky Way from a quantitative analysis of the  $^{12}\text{CO}(1-0)$  line emission and OH absorption lines. Their derived  $^{12}\text{CO}(1-0)$  intensity map and velocity field (Fig. 8 in Sawada et al. 2004) show a remarkable resemblance to the  $^{12}\text{CO}(1-0)$  distribution in NGC 6946, especially when accounting for differences in angular resolution. In both cases, the molecular gas distribution is elongated with an apparent extent of  $500 \text{ pc} \times 200 \text{ pc}$ . Sawada et al. (2004) suggest that in the case of the Milky Way, this gaseous “bar” is actually formed by two barely resolved spiral arms formed as a response to a large-scale stellar bar.

However, there are also important differences. In NGC 6946, the molecular gas appears more concentrated than in the Milky Way. The gas mass  $M_{\text{H}_2}$  contained within the nuclear spiral, i.e. within a radius of 140 pc is about  $9.3 \times 10^7 M_\odot$ . For the Milky Way, Launhardt et al. (2002) have reported a gas mass of  $2 \times 10^7 M_\odot$  within  $r \leq 230$  pc, which implies a gas density about a factor of up to 12 lower than in NGC 6946. The high molecular gas density in the center of NGC 6946, in particular the presence of a massive gas clump at the galaxy nucleus, appears somewhat unusual. In IC 342, another late-type spiral with enhanced star formation, the molecular gas is located in a ring-like structure around the nuclear cluster, but there is little gas inside the about 100 pc diameter ring:  $M_{\text{H}_2} \sim 2 \times 10^5 M_\odot$  in the inner

30 pc (Schinnerer et al. 2003). Most likely, some of these morphological differences are the consequence of time evolution. It is obvious that the currently observed gas distribution can be only a short-lived phenomenon, as the fueling process itself as well as the ongoing star formation impact the gas.

Recently, Bournaud et al. (2005) suggested that large-scale bars in gas-rich spiral galaxies are short-lived. In their dynamical models, the bar almost dissolves within a few dynamical time-scales ( $\sim 1 - 2$  Gyr in their model) due to the angular momentum transfer from the infalling gas to the stellar bar. A similar behavior is expected for inner bars where the dissolution time would be also only a few dynamical time-scales (F. Combes, priv. comm.). Thus, the inner bar of NGC 6946 could significantly weaken within  $10^7$  yr and thus reduce the gas flow. In addition, the (infalling) gas might quickly be used up by the ongoing massive star formation. This together could result in a dearth of molecular gas in the inner few tens of parsec, resulting in a very different appearance of NGC 6946 in the future.

However, if the NIR bar is long-lived, a relaxation oscillator mechanism for (nuclear) starbursts as it has been suggested for the 300 pc ring in the Galactic Center by Stark et al. (2004) could also provide a time-varying molecular gas content. This mechanism is based on the gravitational collapse of the gas into giant gas clouds in the ILR ring suggested by Elmegreen (1994). Stark et al. (2004) used the properties of the Galactic Center molecular gas derived by Martin et al. (2004) to estimate a critical density of  $n(\text{H}_2) \sim 10^{3.5} \text{ cm}^{-3}$  above which the molecular gas in the ILR will become unstable and self-gravitating. The sudden formation of these clouds can result in a starburst. In addition, these larger clouds can then be disrupted by tidal forces and thus inflow to the center can occur. Meier & Turner (2004) have estimated the density of the central cloud E1 which roughly coincides with the CO spiral to  $\sim 10^{4.2} \text{ cm}^{-3}$  showing that a warmer, denser molecular gas is associated with the starburst. In order to test the scenario of a 'relaxation oscillator' for NGC 6946 a better knowledge of the ISM and its properties are required.

Alternatively, the gas distribution might respond strongly to the energetic feedback from the star formation processes. The nuclear cluster in IC 342 experienced its last episode of star formation some 60 Myr ago (Böker, van der Marel, & Vacca 1999b). It seems plausible that the cavity in the molecular gas distribution could be a consequence of that last starburst, either because the intense UV-radiation has destroyed the molecules, or because stellar winds and/or SN explosions have expelled the gas. In contrast, NGC 6946 is actively forming stars, and has been doing so for only  $\sim 7$  Myr (Engelbracht et al. 1996). While it is currently not possible to decide which of the mechanisms discussed here more strongly affects the molecular gas distribution, they both will reduce the amount of molecular gas in the nucleus of NGC 6946. One might thus speculate that in another 50 Myr or so, the central molecular

gas distribution in NGC 6946 will be more similar to the one observed in IC 342.

There is no clear evidence for the presence of an AGN in NGC 6946, although Holt et al. (2003) find two luminous X-ray sources in the vicinity of the nucleus. It is interesting to note that within the errors, the fainter one coincides with our best estimate of the dynamical center (see Fig. 9). Given that this source most likely is subject to the rather high extinction due to the central CO clump, its intrinsic X-ray luminosity could be well above the Eddington limit for a neutron star, providing some tentative evidence for a central black hole in NGC 6946. On the other hand, the X-ray spectrum of the nuclear source is not substantially different from that of the rest of the X-ray source population, and might have another explanation related to the intense nuclear star formation.

## 6. Summary and Conclusions

The sub-arcsecond resolution CO observations presented in this paper resolve for the first time the molecular gas concentration within the inner 300pc of NGC 6946. The molecular gas is located in an S-shaped spiral structure with three high-luminosity clumps located at the dynamical center and on either end of the spiral. Strong streaming motions are associated with the straight gas lanes of this spiral structure and are even observed within the inner few 10 parsec. Supported by simulations of gas orbits in a perturbed mass model of NGC 6946, we conclude that the observed morphology is best explained by the gas responding to the non-axisymmetric potential of an inner, small-scale stellar bar.

We find that a molecular gas mass of  $M_{\text{H}_2} \sim 1.6 \times 10^7 M_{\odot}$  has accumulated within a radius of 27 pc. Although spatially unresolved in our data we find evidence from analysis of the p-v diagrams that the gas inside the nuclear clump is likely distributed in a ring which would then lie close to the ILR of the inner stellar bar. Such a morphology closely resembles that predicted (and observed) for the ILR of large-scale bars. While a direct confirmation of the nuclear gas ring has to await higher resolution data, our analysis suggests that inner bars are indeed capable of funneling gas towards galactic nuclei to within at least a few tens of parsec.

Comparison of the NGC 6946 results to similar studies for the Milky Way and IC 342 indicates that the amount and distribution of molecular gas in the central 100 parsec of NGC 6946 is fairly different and suggests that the molecular gas properties in galactic nuclei might be strongly variable over time. We discuss scenarios where the observed CO properties critically depend on the nuclear star formation history and the (exact) shape of the nuclear stellar potential present at the time of the observations. Our results, however, demonstrate

that - at least in gas-rich spirals - significant amounts of molecular gas can be present in the immediate vicinity ( $r < 60$  pc) of the nucleus; they are likely transported there by an inner bar and - at least a significant fraction - effectively converted into stars. This adds some support to scenarios in which secular evolution plays a significant role for the ongoing morphological evolution of spirals at the late-type end of the Hubble sequence.

We would like to thank J. Knapen and R. de Jong for their quick and constructive feedback on the  $K_s$  band data. In addition, we are grateful to D. Calzetti and M. Sosey for providing the NICMOS images of NGC 6946. We thank the anonymous referee for insightful comments which helped to improve the paper. UL acknowledges support by the Spanish Ministry of Education, via the research projects AYA 2005-07516-C02-01, ESP 2004-06870-C02-02, and the Junta de Andalucía. This paper has benefited from use of the LEDA database (<http://leda.univ-lyon1.fr>). This research has made use of the NASA/IPAC Extragalactic Database (NED) which is operated by the Jet Propulsion Laboratory, California Institute of Technology, under contract with the National Aeronautics and Space Administration.

## REFERENCES

- Athanassoula, E., 1992, MNRAS, 259, 345
- Belley, J., & Roy, J.-R. 1992, ApJS, 78, 61
- Binney, J., Gerhard, O. E., Stark, A. A., Bally, J., & Uchida, K. I. 1991, MNRAS, 252, 210
- Blais-Ouellette, S., Amram, P., Carignan, C., & Swaters, R. 2004, A&A, 420, 147
- Böker, T., Förster-Schreiber, N. M., & Genzel, R. 1997, AJ, 114, 1883
- Böker, T., et al. 1999a, ApJS, 124, 95
- Böker, T., van der Marel, R. P., & Vacca, W. D. 1999b, AJ, 118, 831
- Bournaud, F., Combes, F., & Semelin, B. 2005, MNRAS, 364, L18
- Braine, J., Duc, P.-A., Lisenfeld, U., Charmandaris, V., Vallejo, O., Leon, S., & Brinks, E. 2001, A&A, 378, 51
- Cardelli, J. A., Clayton, G. C., & Mathis, J. S. 1989, ApJ, 345, 245
- Carignan, C., Charbonneau, P., Boulanger, F., & Viallefond, F. 1990, A&A, 234, 43

- Combes, F., & Elmegreen, B. G. 1993, *A&A*, 271, 391
- Combes, F., & Gerin, M. 1985, *A&A*, 150, 327
- Crosthwaite, L. P. 2002, *PASP*, 114, 929
- de Vaucouleurs, G. 1958, *ApJ*, 127, 487
- de Vaucouleurs, G., de Vaucouleurs, A., Corwin, H. G., Buta, R. J., Paturel, G., & Fouque, P. 1992, *VizieR Online Data Catalog*, 7137, 0
- de Vaucouleurs, G., de Vaucouleurs, A., Corwin, H. G., Buta, R. J., Paturel, G., & Fouque, P. 1991, Volume 1-3, XII, 2069 pp. 7 figs.. Springer-Verlag Berlin Heidelberg New York
- Draine, B. T. 2003, *ARA&A*, 41, 241
- Elmegreen, B. G. 1994, *ApJ*, 425, L73
- Elmegreen, B. G., Elmegreen, D. M., & Montenegro 1992, *ApJS*, 79, 37
- Elmegreen, D. M., Chromey, F. R., & Santos, M. 1998, *AJ*, 116, 1221
- Emsellem, E., Monnet, G., & Bacon, R. 1994, *A&A*, 285, 723
- Emsellem, E., Goudfrooij, P., & Ferruit, P. 2003, *MNRAS*, 345, 1297
- Engelbracht, C. W., Rieke, M. J., Rieke, G. H., & Latter, W. B. 1996, *ApJ*, 467, 227
- Engelbracht, C. W., Rieke, M. J., Rieke, G. H., Kelly, D. M., & Achtermann, J. M. 1998, *ApJ*, 505, 639
- Englmaier, P. & Shlosman, I. 2000, *ApJ*, 528, 677
- Garcia-Burillo, S., Sempere, M. J., Combes, F., & Neri, R. 1998, *A&A*, 333, 864
- García-Burillo, S., et al. 2003, *A&A*, 407, 485
- Gebhardt, K., et al. 2000, *ApJ*, 539, L13
- Genzel, R., Hollenbach, D., & Townes, C. H. 1994, *Reports of Progress in Physics*, 57, 417
- Guilloteau, S., & Lucas, R. 2000, *ASP Conf. Ser.*, 217, 299
- Güsten, R. 1989, *IAU Symp. 136: The Center of the Galaxy*, 136, 89

- Helfer, T. T., Thornley, M. D., Regan, M. W., Wong, T., Sheth, K., Vogel, S. N., Blitz, L., & Bock, D. C.-J. 2003, *ApJS*, 145, 259
- Ho, L. C., Filippenko, A. V., & Sargent, W. L. W. 1997, *ApJS*, 112, 315
- Holt, S. S., Schlegel, E. M., Hwang, U., & Petre, R. 2003, *ApJ*, 588, 792
- Ishizuki, S., Kawabe, R., Ishiguro, M., Okumura, S. K., Morita, K.-I., Chikada, Y., Kasuga, T., & Doi, M. 1990, *ApJ*, 355, 436
- Jarrett, T. H., Chester, T., Cutri, R., Schneider, S. E., & Huchra, J. P. 2003, *AJ*, 125, 525
- Karachentsev, I. D., Sharina, M. E., & Huchtmeier, W. K. 2000, *A&A*, 362, 544
- Kennicutt, R. C. 1983, *ApJ*, 272, 54
- Knapen, J. H., de Jong, R. S., Stedman, S., & Bramich, D. M. 2003, *MNRAS*, 344, 527
- Kormendy, J. & Kennicutt, R. C. 2004, *ARA&A*, 42, 603
- Krabbe, A., Sternberg, A., & Genzel, R. 1994, *ApJ*, 425, 72
- Larsen, S. S., & Richtler, T. 1999, *A&A*, 345, 59
- Launhardt, R., Zylka, R., & Mezger, P. G. 2002, *A&A*, 384, 112
- Maciejewski, W. 2004a, *MNRAS*, 354, 883
- Maciejewski, W. 2004b, *MNRAS*, 354, 892
- Maciejewski, W., Teuben, P. J., Sparke, L. S., & Stone, J. M. 2002, *MNRAS*, 329, 502
- Martin, C. L., Walsh, W. M., Xiao, K., Lane, A. P., Walker, C. K., & Stark, A. A. 2004, *ApJS*, 150, 239
- Meier, D. S. & Turner, J. L. 2004, *AJ*, 127, 2069
- Menéndez-Delmestre, K., Sheth, K., Scoville, N.Z., Jarrett, T., Schinnerer, E., Regan, M. 2006, in prep.
- Monnet, G., Bacon, R., & Emsellem, E. 1992, *A&A*, 253, 366
- Osterbrock, D. E. 1989, *Astrophysics of Gaseous Nebulae and Active Galactic Nuclei* (Mill Valley: University Science Books)

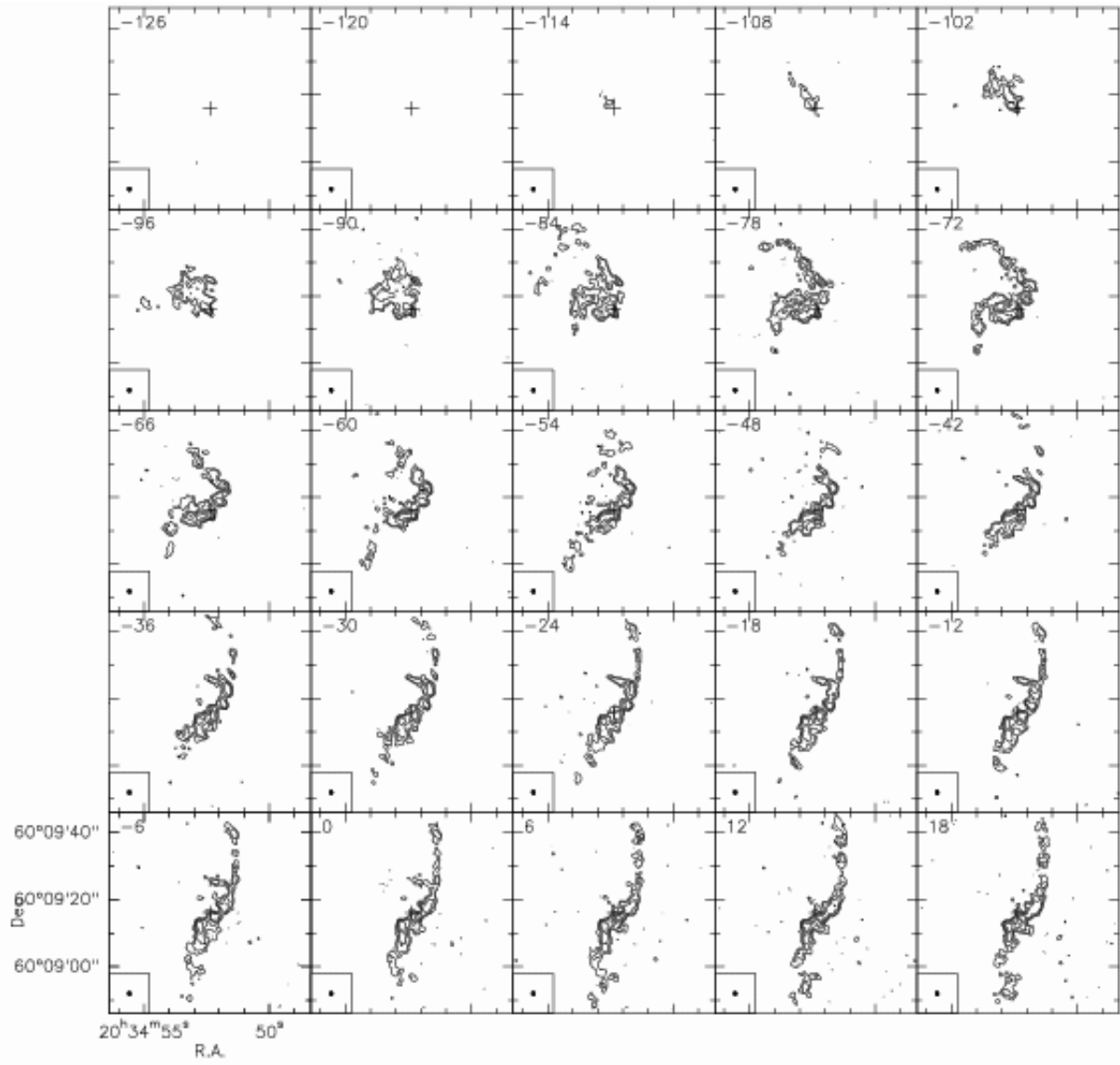
- Paturel, G., Petit, C., Prugniel, P., Theureau, G., Rousseau, J., Brouty, M., Dubois, P., & Cambrésy, L. 2003, *A&A*, 412, 45
- Pisano, D. J., & Wilcots, E. M. 2000, *MNRAS*, 319, 821
- Quillen, A. C. & Yukita, M. 2001, *AJ*, 121, 2095
- Regan, M. W. & Vogel, S. N. 1995, *ApJ*, 452, L21
- Regan, M. W., Thornley, M. D., Helfer, T. T., Sheth, K., Wong, T., Vogel, S. N., Blitz, L., & Bock, D. C.-J. 2001, *ApJ*, 561, 218
- Sakamoto, K., Baker, A. J., & Scoville, N. Z. 2000, *ApJ*, 533, 149
- Sakamoto, K., Okumura, S. K., Ishizuki, S., & Scoville, N. Z. 1999, *ApJS*, 124, 403
- Sawada, T., Hasegawa, T., Handa, T., & Cohen, R. J. 2004, *MNRAS*, 349, 1167
- Schinnerer, E., Böker, T., & Meier, D. S. 2003, *ApJ*, 591, L115
- Schinnerer, E., Maciejewski, W., Scoville, N., & Moustakas, L. A. 2002, *ApJ*, 575, 826
- Schmidt, B. P., Kirshner, R. P., Eastman, R. G., Maza, J., & Aviles, R. 1994, *ApJ*, 432, 42
- Sheth, K., Vogel, S. N., Regan, M. W., Teuben, P. J., Harris, A. I., & Thornley, M. D. 2002, *AJ*, 124, 2581
- Sheth, K., Regan, M. W., Vogel, S. N., & Teuben, P. J. 2000, *ApJ*, 532, 221
- Sheth, K., Vogel, S. N., Regan, M. W., Thornley, M. D., & Teuben, P. J. 2005, *ApJ*, 632, 217
- Stark, A. A., Martin, C. L., Walsh, W. M., Xiao, K., Lane, A. P., & Walker, C. K. 2004, *ApJ*, 614, L41
- Strong, A. W., et al. 1988, *A&A*, 207, 1
- Swaters, R. A. 1999, Ph.D. Thesis, Rijksuniversiteit Groningen
- Tacconi-Garman, L. E., Sternberg, A., & Eckart, A. 1996, *AJ*, 112, 918
- Tully, R.B., 1988, "Nearby Galaxies Catalog", Cambridge, Cambridge University Press
- Wada, K. & Koda, J. 2001, *PASJ*, 53, 1163

Walsh, W., Beck, R., Thuma, G., Weiss, A., Wielebinski, R., & Dumke, M. 2002, A&A, 388,  
7

Table 1.  $^{12}\text{CO}(1-0)$  fluxes and Molecular Gas Masses

| Component      | $S_{\text{CO}}$<br>[Jy km s $^{-1}$ ] | $M_{\text{H}_2}$<br>[ $10^7 M_{\odot}$ ] |
|----------------|---------------------------------------|--|
| total          | 1310                                  | 30.98                                    |
| Nuclear spiral | 394                                   | 9.31                                     |
| Nuclear Clump  | 67                                    | 1.58                                     |
| Clump North    | 31                                    | 0.74                                     |
| Clump South    | 101                                   | 2.38                                     |
| Central 4''    | 95                                    | 2.25                                     |

Note. —  $^{12}\text{CO}(1-0)$  line fluxes and molecular gas masses for various components of the molecular gas distribution derived from the primary beam corrected data. The components are indicated in Fig. 5. Note that the molecular gas masses could be lower by up to a factor of about 4 – 5 due to the uncertainty in the conversion factor  $X_{\text{CO}}$  (see text). The Helium fraction of 36% has not been taken into account for the values of  $M_{\text{H}_2}$ .



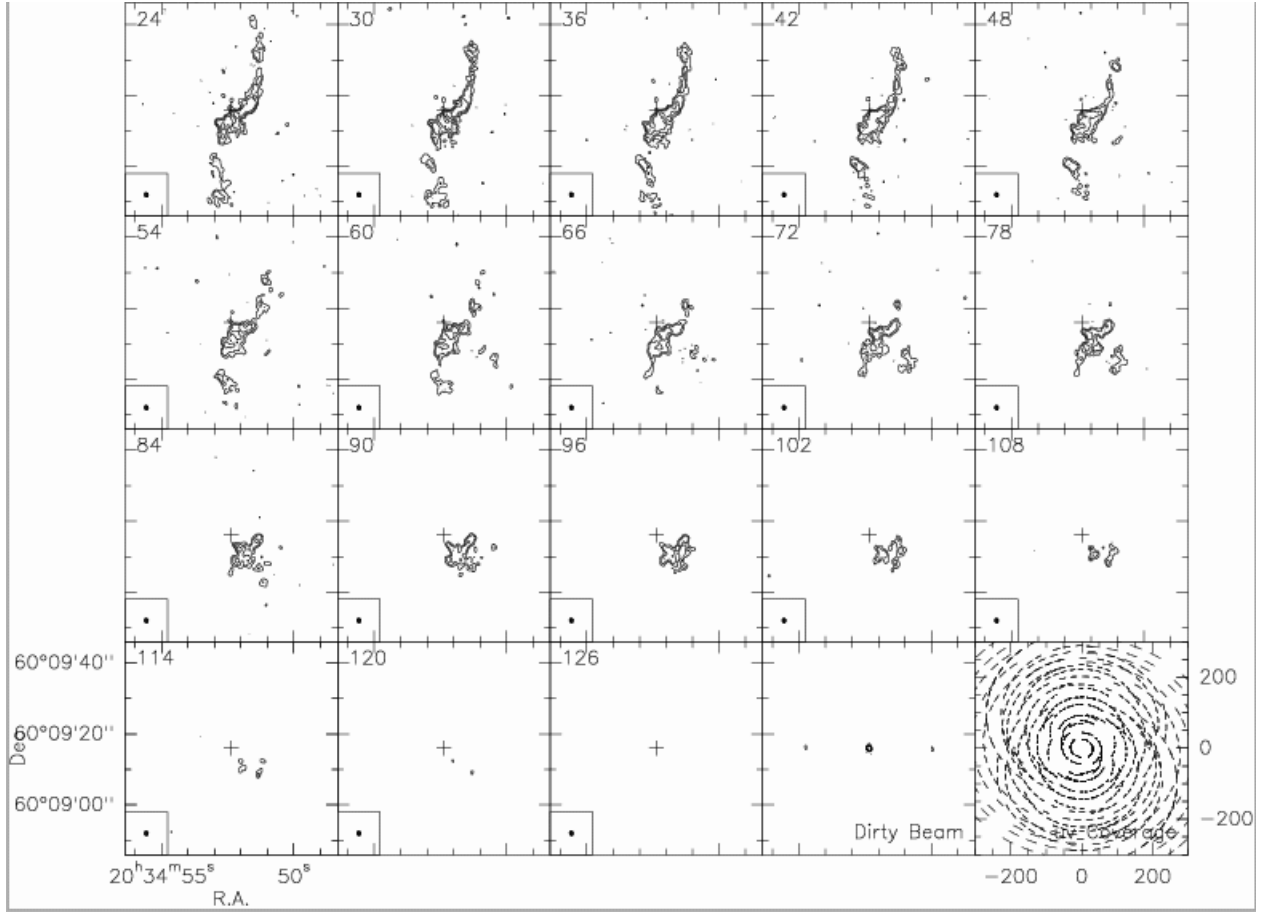


Fig. 1.— Channel maps of the  $^{12}\text{CO}(1-0)$  line. The channels are  $6 \text{ km s}^{-1}$  wide, and contours are plotted at  $5, 10, 20, 40\sigma$  with  $1\sigma = 4 \text{ mJy/beam}$ . The velocity marking (top left corner) is relative to the observed central velocity of  $v = 65 \text{ km s}^{-1}$ . The CLEAN beam of  $1.25'' \times 1.01''$  is shown in the bottom left corner of each channel. The dirty beam and the  $uv$  coverage are shown in the last two channels.



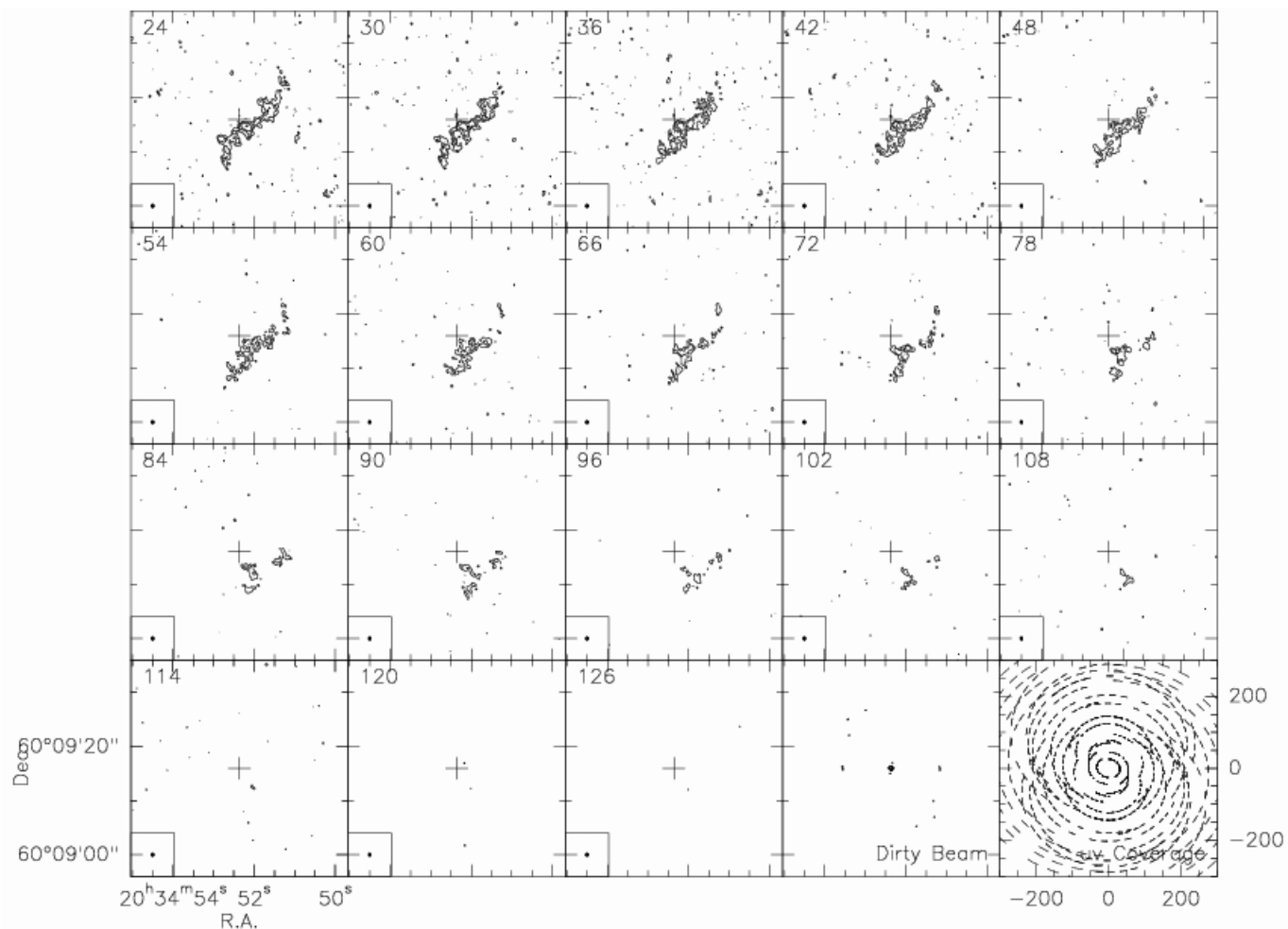


Fig. 2.— Channel maps of the  $^{12}\text{CO}(2-1)$  line. The channels are  $6 \text{ km s}^{-1}$  wide, and contours are plotted at  $3, 6, 12, 24\sigma$  with  $1\sigma = 12 \text{ mJy/beam}$ . The velocity marking (top left corner) is relative to the observed central velocity of  $v = 65 \text{ km s}^{-1}$ . The CLEAN beam of  $0.58'' \times 0.48''$  is shown in the bottom left corner of each channel. The dirty beam and the  $uv$  coverage are shown in the last two channels.

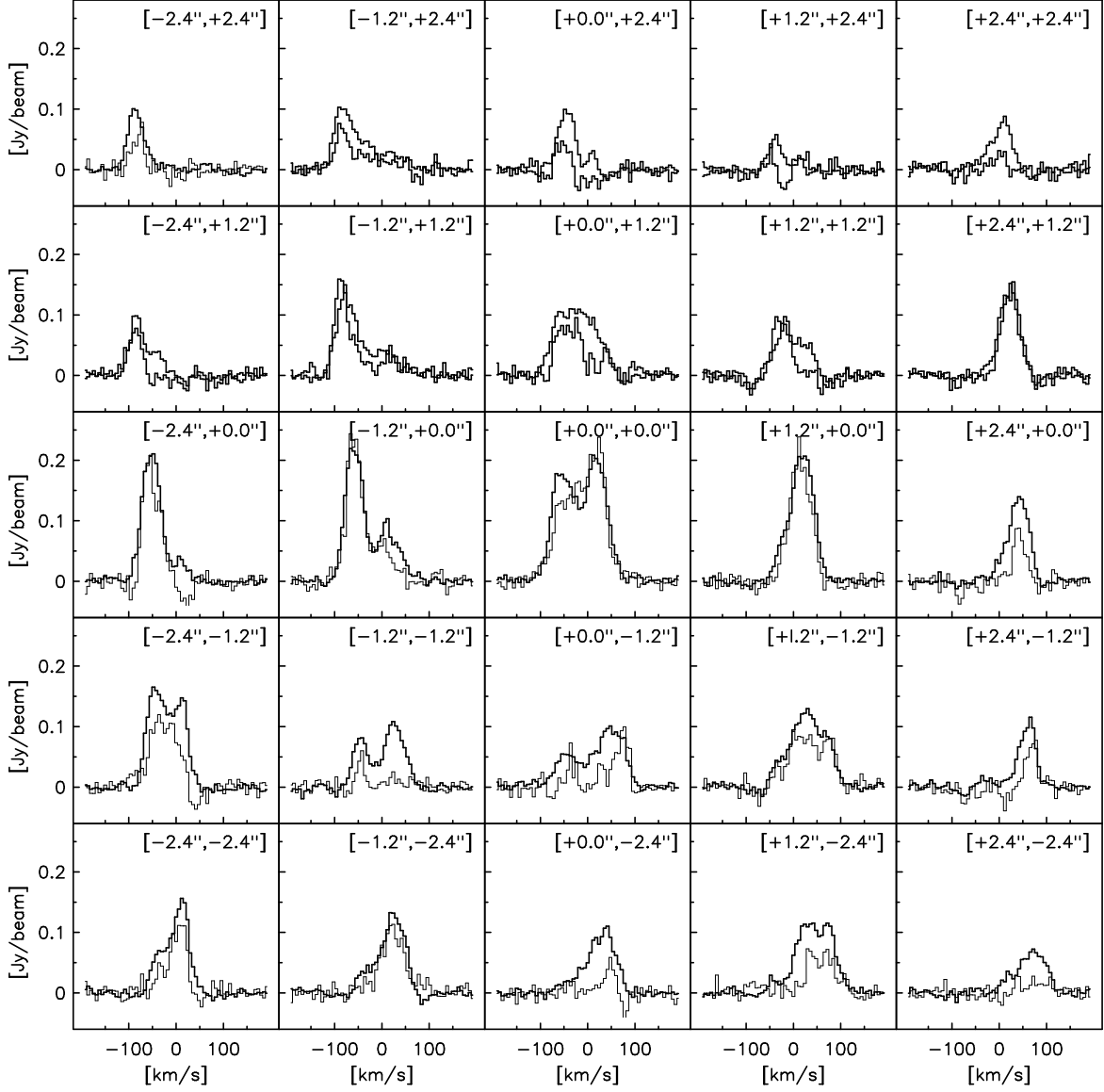


Fig. 3.— Spectra of the  $^{12}\text{CO}(1-0)$  (*heavy solid line*) and  $^{12}\text{CO}(2-1)$  (*thin solid line*) line emission extracted with in the central  $4.8'' \times 4.8''$  around the dynamical center (see § 3.2). The spectra have not been corrected for the different beam sizes.

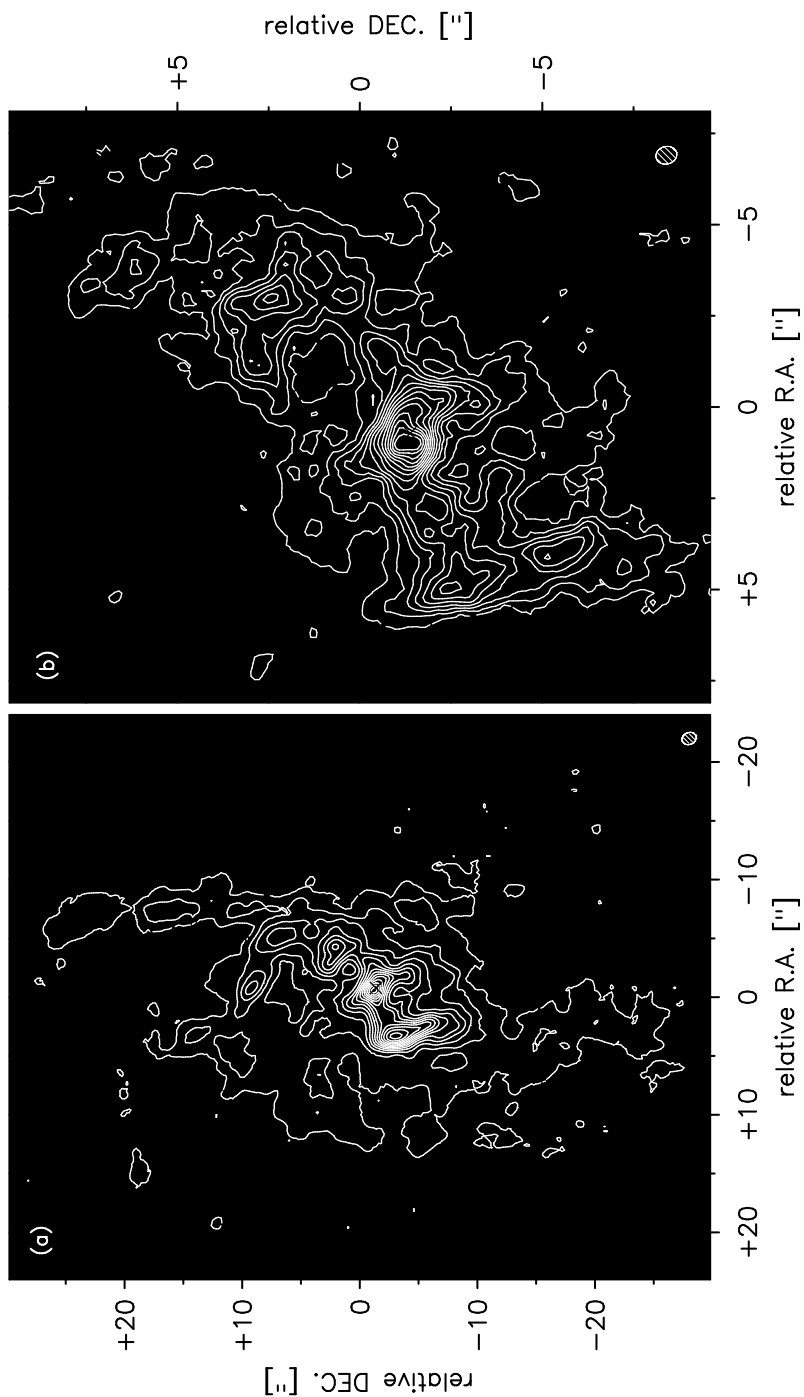


Fig. 4.— Intensity maps of the  $^{12}\text{CO}(1-0)$  (a) and  $^{12}\text{CO}(2-1)$  (b) lines. The coordinates are relative to the phase center of the observations. The dynamical center inferred from the kinematics (see § 3.2) is marked with a cross in both panels. The contour levels are 0.60, 2.28, 3.96, ...  $\text{Jy km s}^{-1}$  and 1.26, 2.94, 4.62, ...  $\text{Jy km s}^{-1}$  for the  $^{12}\text{CO}(1-0)$  and  $^{12}\text{CO}(2-1)$  emission.

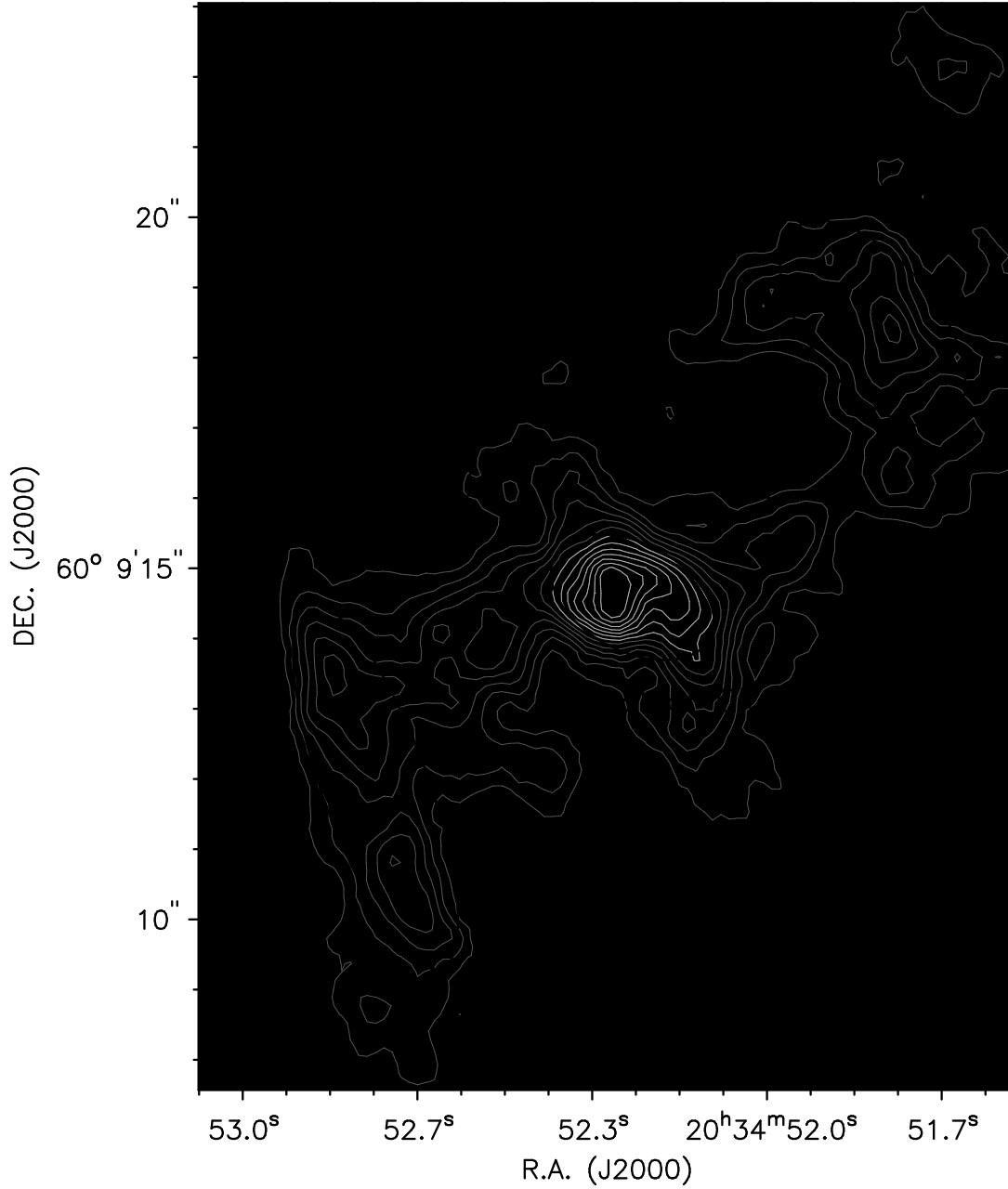


Fig. 5.—  $^{12}\text{CO}(2 - 1)$  intensity map (*gray-scale, grey contours*) showing the nuclear spiral structure. The important features described in the text (see § 3.4) are indicated. The ellipses roughly outline the areas used to derived the  $^{12}\text{CO}(1 - 0)$  line flux and thus the molecular gas mass (see § 3.4 and Tab.1). The CLEAN beam is shown in the bottom left corner.

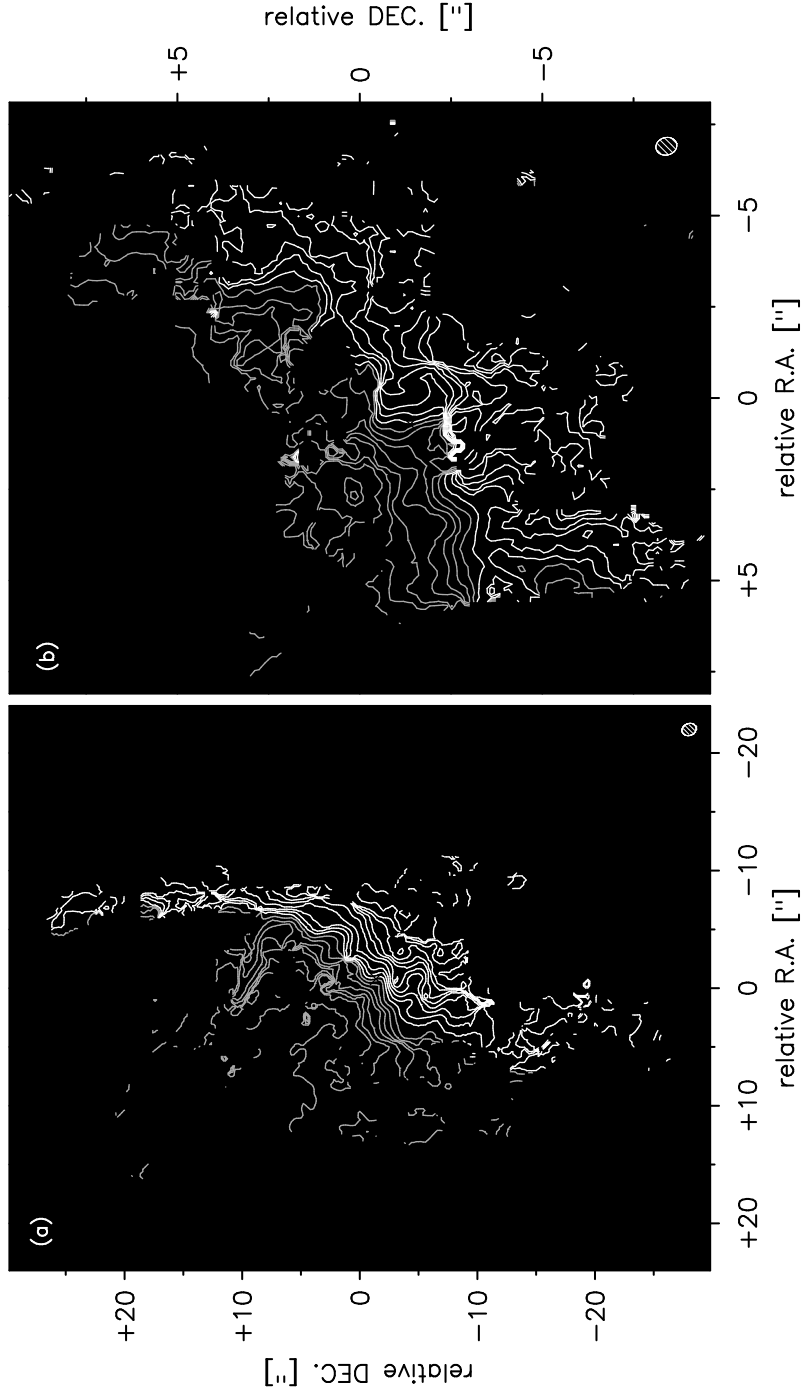


Fig. 6.— Velocity fields of the  $^{12}\text{CO}(1-0)$  (a) and  $^{12}\text{CO}(2-1)$  (b) lines. The coordinates are relative to the phase center of the observations. The dynamical center inferred from the kinematics (see § 3.2) is marked with a cross in both panels. The iso-velocity contours are in steps of  $10 \text{ km s}^{-1}$  starting from  $+5 \text{ km s}^{-1}$  (positive; white contours) and  $-5 \text{ km s}^{-1}$  (negative; grey contours) relative to the systemic velocity of  $v_{sys}(LSR) = 50 \text{ km s}^{-1}$  (see §3.2).

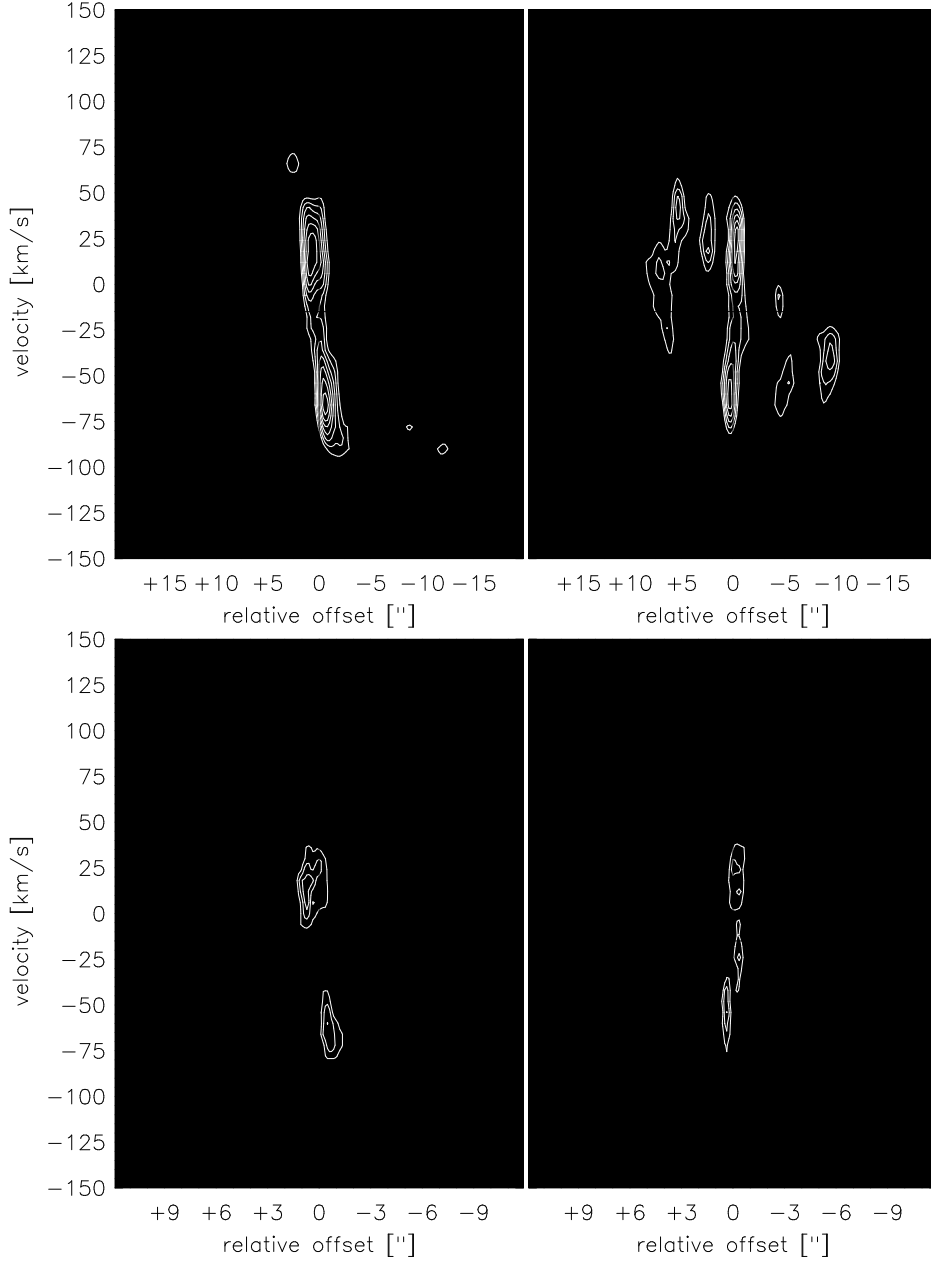


Fig. 7.— Position-velocity (p-v) diagrams of the  $^{12}\text{CO}(1-0)$  (*top*) and  $^{12}\text{CO}(2-1)$  (*bottom*) line emission along the major kinematic axes (*a*, *c*) and the minor kinematics axes (*b*, *d*). The contours start at  $3\sigma=12\text{mJy/beam}$  and are in steps of  $3\sigma$  till  $24\sigma$  when they continue in steps of  $6\sigma$  for the  $^{12}\text{CO}(1-0)$  p-v diagrams (*a*, *b*), and they start at  $3\sigma=30\text{mJy/beam}$  and are in steps of  $3\sigma$  for the  $^{12}\text{CO}(2-1)$  ones (*b*, *d*). The solid horizontal line corresponds to the systemic velocity of  $v_{sys}(LSR) = 50 \text{ km s}^{-1}$ .

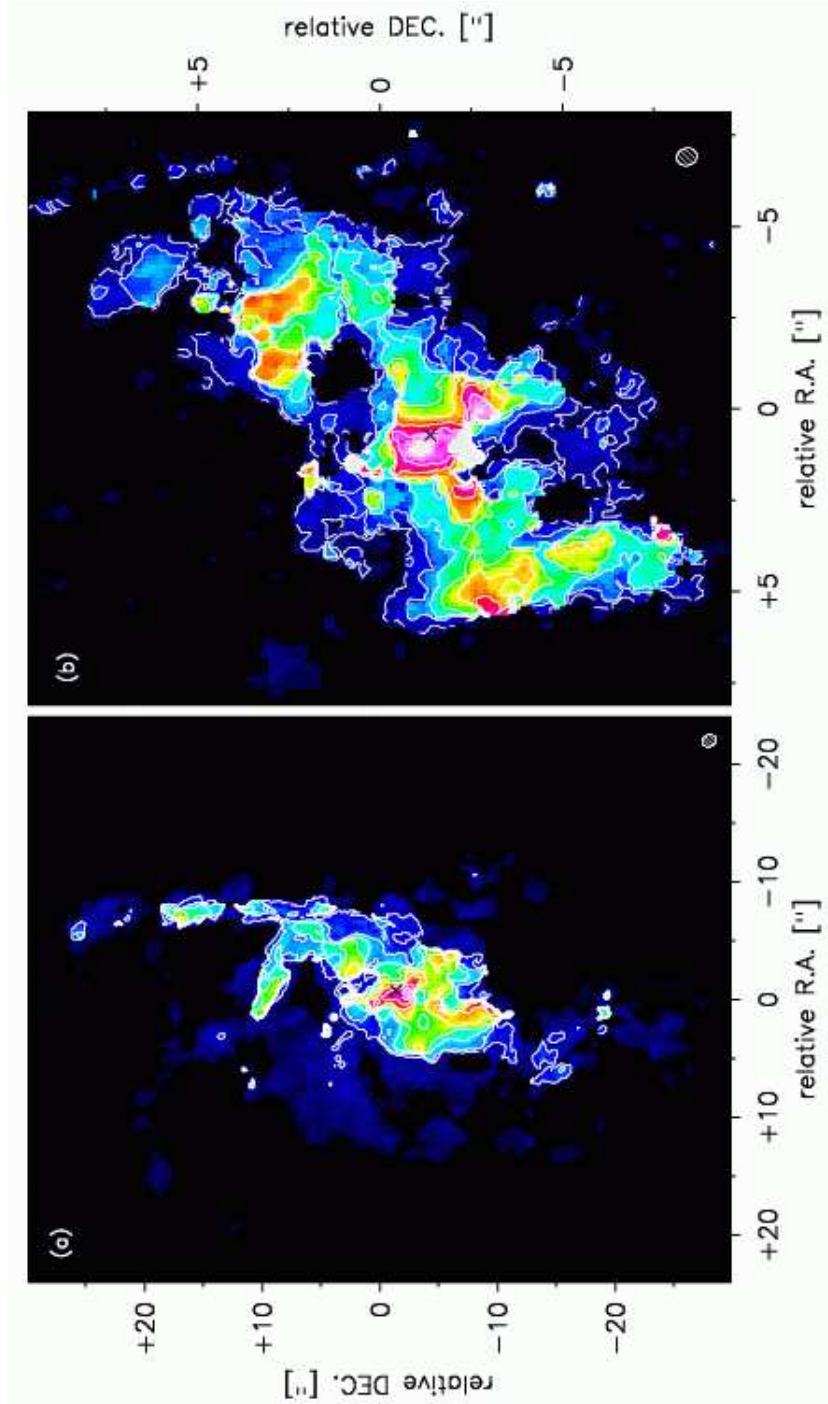


Fig. 8.— Dispersion maps of the  $^{12}\text{CO}(1-0)$  (a) and  $^{12}\text{CO}(2-1)$  (b) lines. The coordinates are relative to the phase center of the observations. The dynamical center inferred from the kinematics (see § 3.2) is marked with a cross in both panels. The contours start at  $10\text{ km s}^{-1}$  and  $5\text{ km s}^{-1}$  for the  $^{12}\text{CO}(1-0)$  and  $^{12}\text{CO}(2-1)$  line with steps of  $5\text{ km s}^{-1}$ .

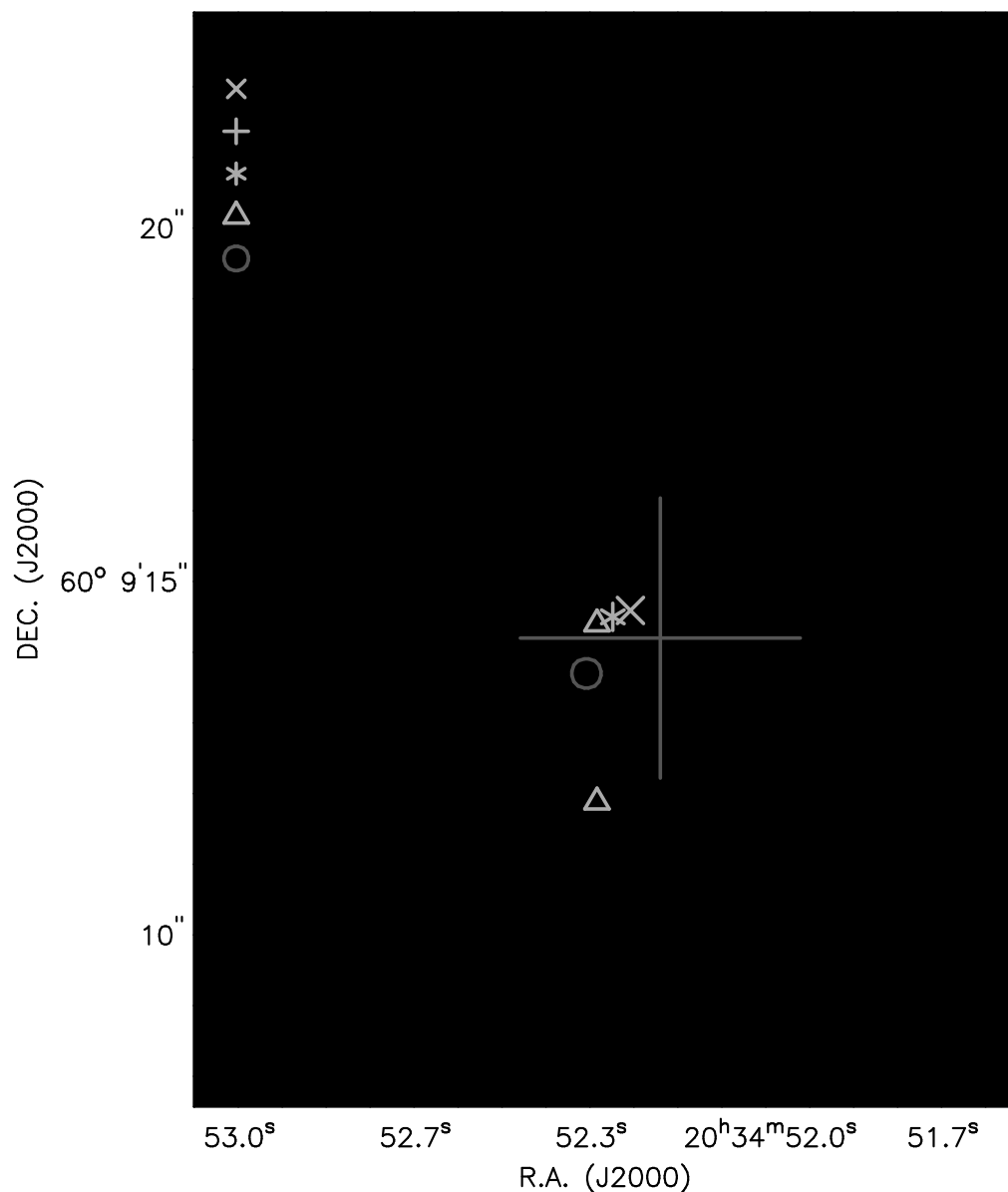


Fig. 9.— Location of the dynamical center as derived from our data ( $^{12}\text{CO}(2-1)$  intensity map in grey-scale), compared to that derived from observations made with the OVRO mm-interferometer (Meier & Turner 2004). Also indicated are the positions of the 2 cm radio continuum peak (Turner & Hurt 1983) and two nuclear X-ray sources identified by Holt et al. (2003). In addition, the position of the 2MASS center from Meier & Turner (2004) is shown. The size of the symbol represents the positional uncertainty, except for the X-ray sources. The solid lines indicate the orientation of the position-velocity cuts presented in Fig. 13. The CLEAN beam is shown in the bottom left corner.

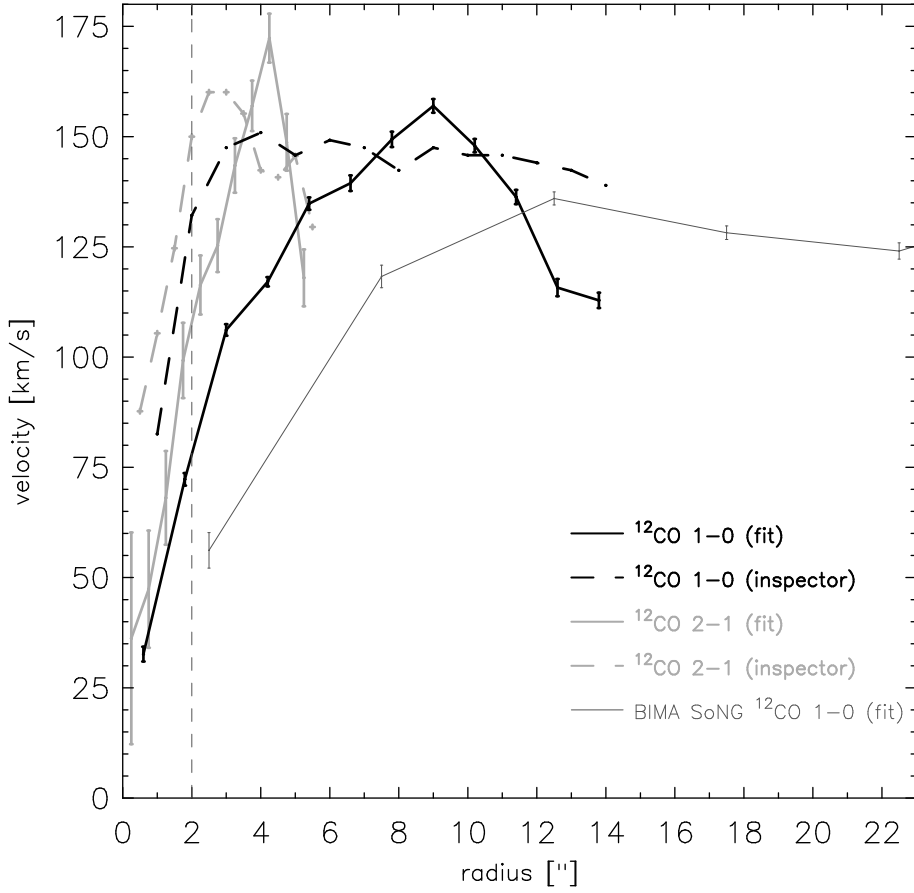


Fig. 10.— Rotation curves of the molecular gas within a radius of  $\sim 500$  pc from the nucleus of NGC 6946. The derived deprojected velocities for the  $^{12}\text{CO}(1-0)$  and  $^{12}\text{CO}(2-1)$  line from the PdBI and BIMA data are shown. The steepening of the gradient within the first  $6''$  is due to the higher angular resolution of the  $^{12}\text{CO}(2-1)$  data and the fact that the 'INSPECTOR' derived rotation curves are less affected by beam smearing (see § 3.3 for details). The error bars for the 'ROTCUR' derived rotation curves represent the uncertainties from the least-square fit. The  $^{12}\text{CO}(1-0)$  rotation curve of the BIMA SoNG data shows that the apparent drop in the PdBI CO rotation curves is an artifact due to insufficient sampling at larger radii. The dashed line marks the radius of  $2''$  used to derive the dynamical mass in § 3.4.

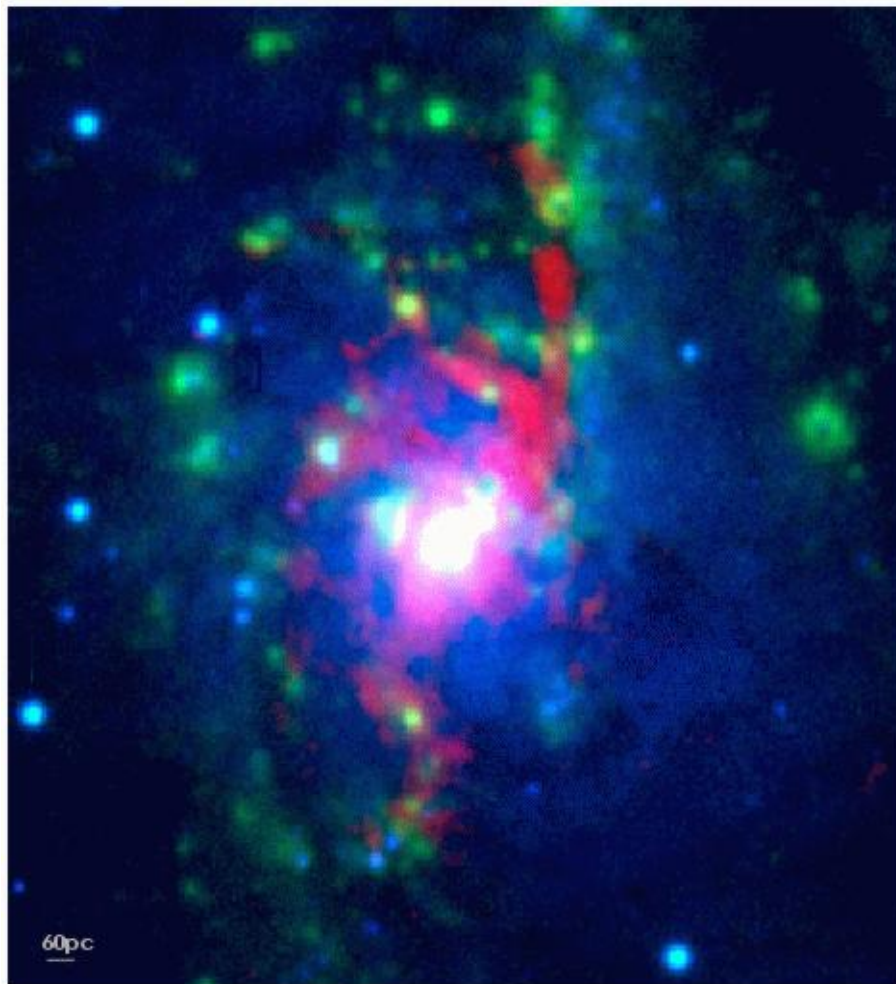


Fig. 11.— Three color composite image of the central arcminute in NGC 6946 showing the  $^{12}\text{CO}(1-0)$  line emission (*red*), the  $\text{H}\alpha$  line emission (*green*) and the I band continuum (*blue*) from the NOT telescope (Larsen & Richtler 1999). The offset between the  $\text{H}\alpha$  and  $^{12}\text{CO}(1-0)$  line emission along the northern straight gas lane is very reminiscent of what has been commonly observed for gas and dust lanes along the leading side of large-scale stellar bars (Sheth et al. 2002).

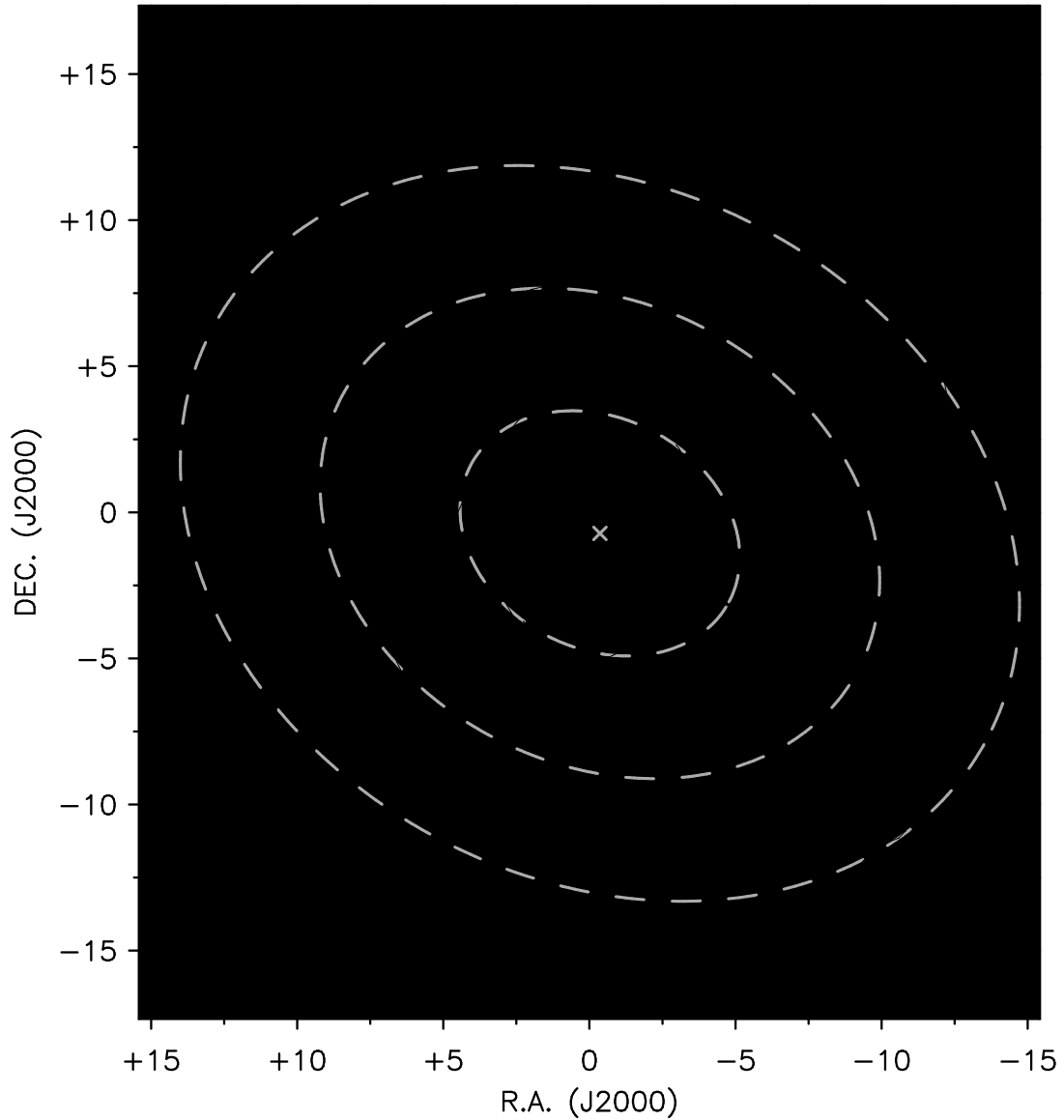


Fig. 12.— Overlay of the  $K_s$  band isophotes from the Knapen et al. (2003) image onto the  $^{12}\text{CO}(2-1)$  intensity map (grey-scale). The extent of the stellar bar ( $4''$ ) as determined by Elmegreen et al. (1998) is shown as a dashed ellipse. The grey dashed ellipses describe circles within the plane of the galaxy with radii of  $5''$ ,  $10''$ , and  $15''$ . The cross marks the location of the dynamical center as described in § 3.3. For further explanation see § 4.2.

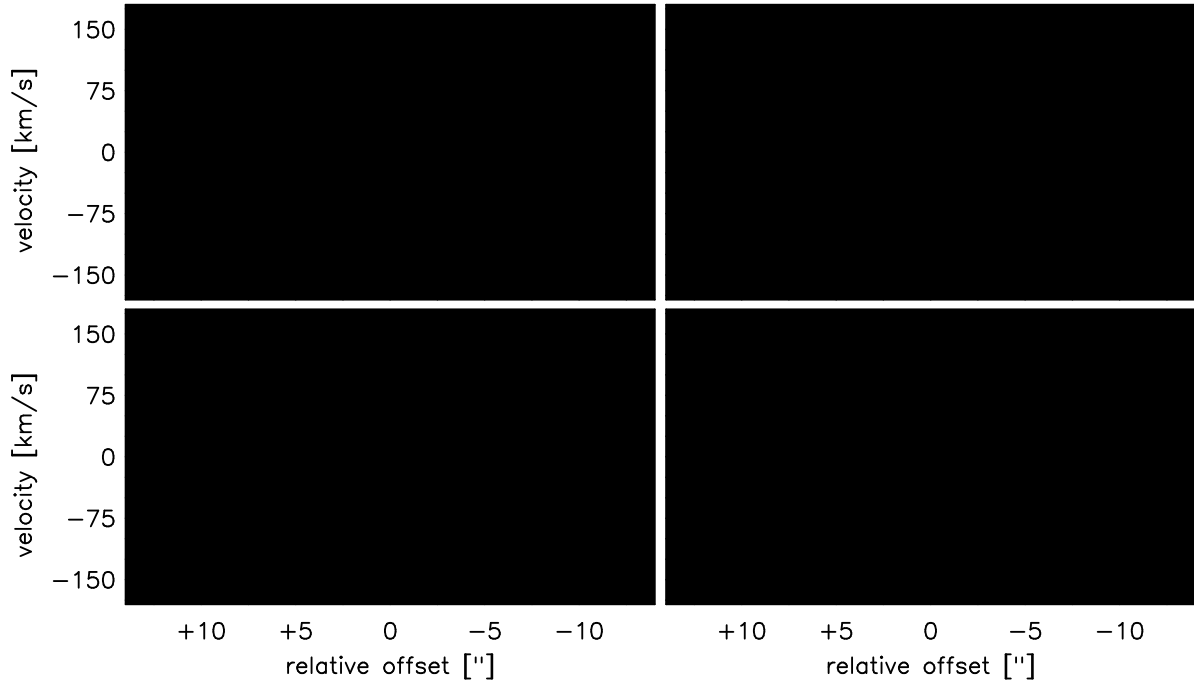


Fig. 13.—  $^{12}\text{CO}(1 - 0)$  position-velocity diagrams for two positions perpendicular to the southern (*right*) and northern (*left*) straight gas lanes (indicated in Fig. 9). (See text for more details.)

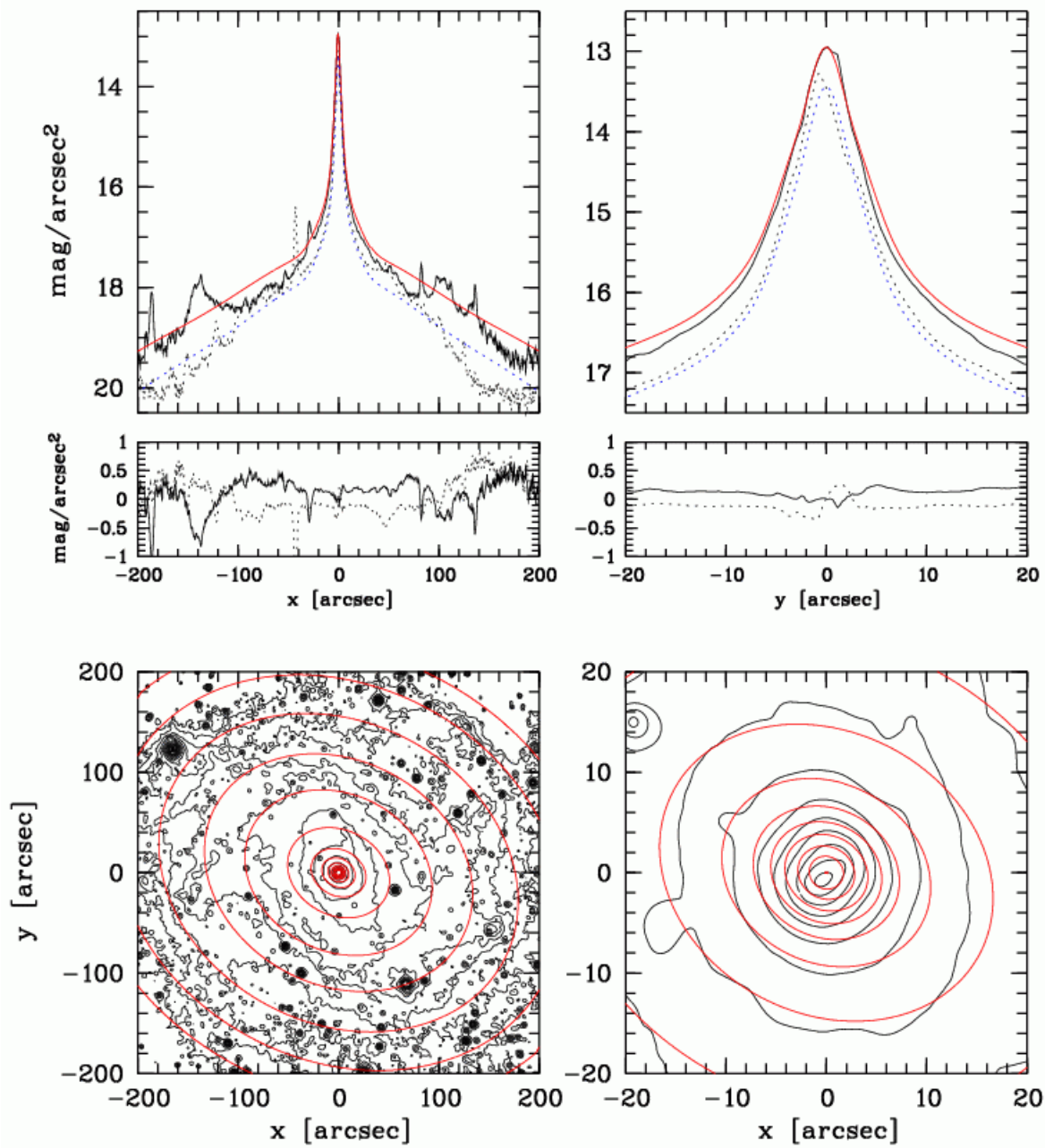


Fig. 14.— Comparison between the  $K_s$  band image and an axisymmetric luminosity model built using the MGE formalism (see text for details). *Top*: North-South (solid:  $K_s$  band, red: MGE model) and East-West (dotted:  $K_s$  band, blue: MGE model) cuts for the central 200'' (*left*) and 20'' (*right*). *Middle*: Residuals between the model and the data. Larger discrepancies are due to the large-scale bar (*left*) and the depression of emission due to the high extinction in the nucleus (*right*) which are not taking into account in the axisymmetric model. *Bottom*: isophotes of the  $K_s$  band images (black contours) and of the MGE model (red contours).

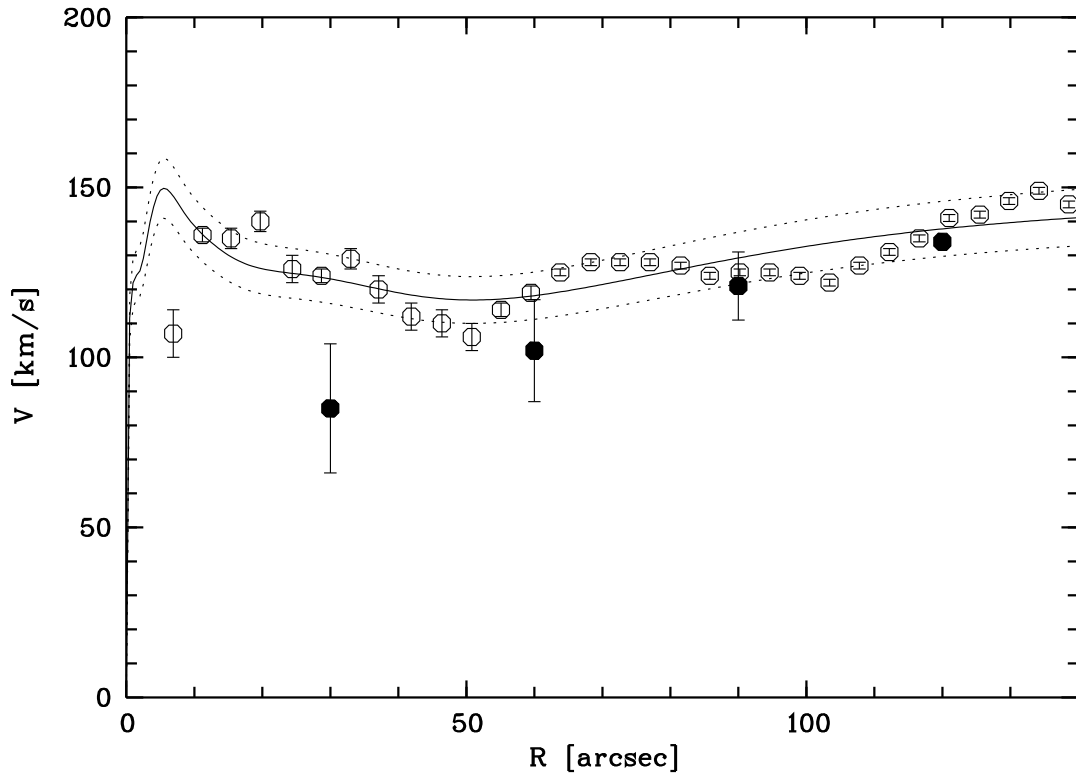


Fig. 15.— Comparison between the observed (deprojected) HI (*filled circles*) and H $\alpha$  (*open circles*) rotation curves in the central 140'' of NGC 6946, and the circular velocity profile derived from the MGE model for  $M/L_K$  of 0.72 (*solid lines*), 0.64 and 0.81 (*dashed lines*).

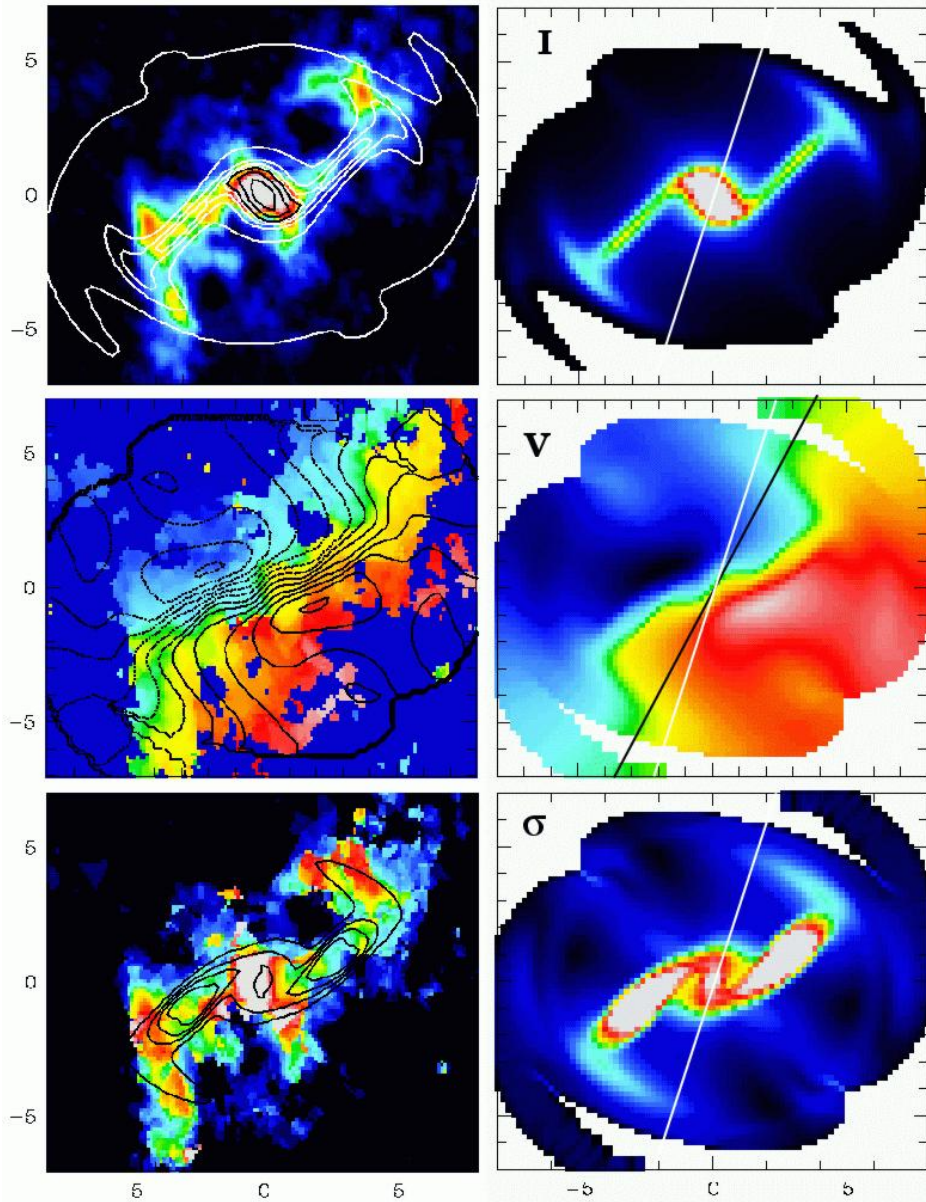


Fig. 16.— Comparison between the intensity maps (*top*), the velocity fields (*middle*) and the velocity dispersion maps (*bottom*) of the gas component of the barred MGE model (*right*: color, *left*: contours) and the observed  $^{12}\text{CO}(2-1)$  line emission (*left*: color). In the *right* panels, we indicate the apparent position angle of the bar in the model (white dashed line) and the line-of-nodes of the unperturbed axisymmetric potential (black dotted line). See text for details.

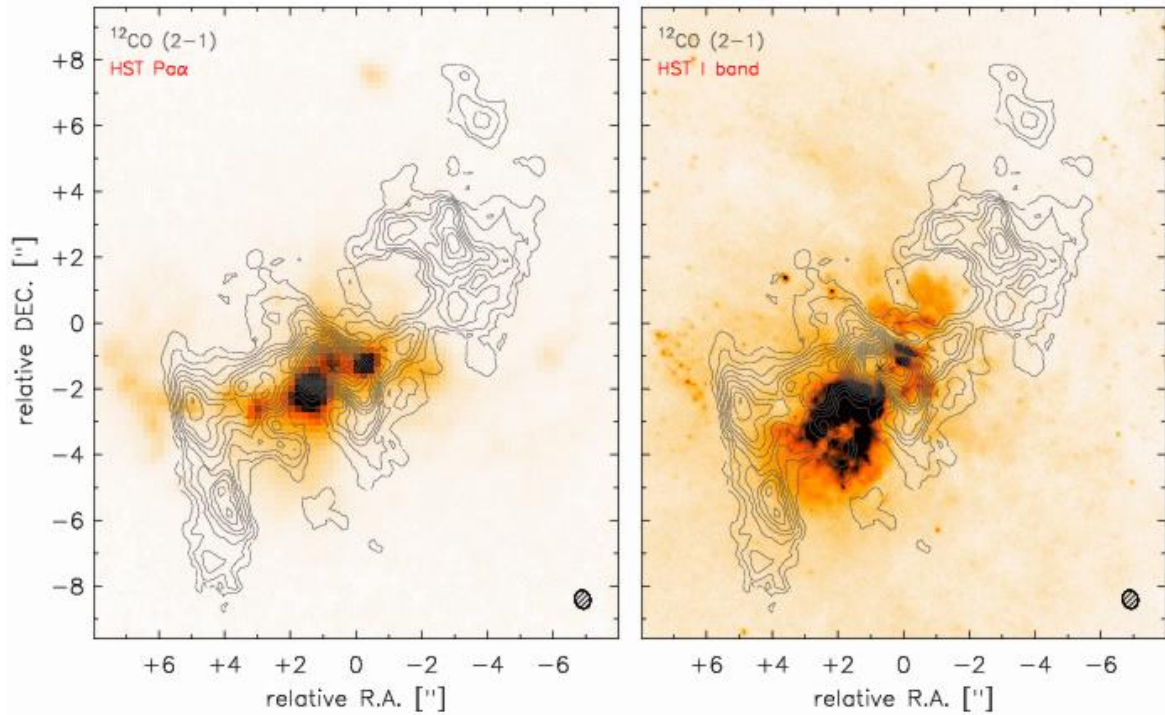


Fig. 17.— Comparison of the CO distribution to HST maps of the stellar light as traced by the I-band continuum (*left*) and the current star formation as traced by the emission of the Pa $\alpha$  recombination line (*right*). In both panels, the cross marks the location of the dynamical center as discussed in § 3.2. The dynamical center (and the highest CO luminosity and likely density) is located in a region of extreme extinction.